Research Paper

Refined Plate Theory for Critical Buckling Analysis of FG Sandwich Nanoplates Considering Neutral Surface Concept and Piezoelectric Surface Effects

A.H. Soltan Arani [1], A. Ghorbanpour Arani [1,2*], Z. Khoddami Maraghi [3]

[1] Department of Solid Mechanics, Faculty of Mechanical Engineering, University of Kashan, Kashan, Iran
[2] Institute of Nanoscience & Nanotechnology, University of Kashan, Kashan, Iran
[3] Faculty of Engineering, Mahallat Institute of Higher Education, Mahallat, Iran

ABSTRACT

The nonlocal quasi-3D static stability analysis of the sandwich simply supported nanoplates embedded in an orthotropic Pasternak foundation placed in an electrical environment by considering the surface effects based on a five-variable refined plate theory by taking into account the stretching effects is investigated in the current study. The core of the structure is functionally graded along its thickness using a power law model. The concept of neutral surface position is applied to achieve symmetry in the distribution of material properties across the thickness. The piezoelectric face sheets are actuators and sensors for the functionally graded layer based on the surface piezoelasticity theory. According to the nonlocal strain gradient theory, the higher-order shear deformation theory is utilized to develop the linear equilibrium equations of motion based on the principle of minimum potential energy. Eventually, a Navier-type solution is applied to obtain the analytical results of a three-layered nano-plate subjected to the electric field. Evaluation of the accuracy and efficiency of the current approach demonstrates a good agreement between the obtained results from this model and those published in the reviewed literature. Eventually, a comprehensive study is conducted to examine the influences of various parameters on the critical buckling load of the functionally graded sandwich structure in detail. Numerical results indicate significant influences of residual surface stress and neutral surface position on the critical buckling load, particularly in thick nanoplates. These findings are expected to aid in designing micro/nano-electro-mechanical system components based on smart nanostructures.

Keywords: Critical Buckling Load; Neutral Surface Concept; Nonlocal Strain Gradient Theory; Surface Effect, Refined Plate Theory.

* Corresponding author. Tel.: +98 31 55913434; Fax: +98 31 55913444.
E-mail address: aghorabn@kashanu.ac.ir (A. Ghorbanpour Arani)

.

1 INTRODUCTION

D EVELOPMENT and advancement in various industries including aerospace and thermal power plants caused by the requirement for materials with high thermal and mechanical strength is more taken into consideration than ever before. Functionally graded materials (FGM) are inhomogeneous materials including two or more various materials by varying the microstructure from one material to another material with a specific gradient. Their dating as an engineering concept reaches the last quarter of the 20th century. The aircraft and aerospace industry, the computer circuit industry, and the fabrication of electrical, electrochemical as well as biomaterials devices are examples of the use of these materials. FGMs as materials with improved properties have attracted the attention of many researchers [1-7]. Piezoelectric materials are materials that can generate internal electrical charge from applied mechanical stress. As well as in the reverse direction, they can create a strain when subjected to an electric field. These technologies are used as actuators and sensors due to the excellent mechanical properties and tunable electric properties in a wide range of applied devices and products in modern societies especially. Thus far, many researchers have focused their research on studying and investigating the behavior of piezoelectric materials [8-13].

A multi-layered plate is a special form of a sandwich structure comprising a combination of different laminates that are bonded to each other so that its properties are considered as the properties of an integrated structure. The primary advantage of multi-layered plates is very high stiffness-to-weight and high bending strength-to-weight ratio. Lightweight and stiff laminated panels are vital elements of many modern civil, aircraft, and spacecraft designs. Subsequently, researchers started to investigate the behavior of the multi-layered structures in the last few years.

Cao et al. [14] studied dynamic analysis of viscoelastically subjected to moving loads using the multi-layer moving plate method. They extracted the governing equations of the connected double-plate system by using the Reissner-Mindlin plate theory. Ragb and Matbuly [15] introduced different numerical schemes to formulate and solve nonlinear vibration analysis of elastically supported multilayer composite plates resting on the Winkler-Pasternak foundation by a first-order shear deformation theory (FSDT). The obtained results show that the used method is an accurate efficient model in the dynamic analysis of discontinuity structure resting on a nonlinear elastic foundation. Taghizadeh et al. [16] investigated the mechanical behavior of novel multi-layer sandwich panels subjected to indentation of a spherical indenter load experimentally and numerically. Amoozgar et al. [17] employed a combining a two-dimensional a one-dimensional nonlinear beam analysis to study the influences of initial curvature and lattice core shape on the vibration of sandwich beams. They used a time-space scheme to obtain nonlinear governing equations of the sandwich beam. Their results show that the lattice unit cell shape affects both in-plane and out-of-plane stiffness and results in changes in the dynamic behavior of the beam. Sahoo et al. [18] predicted nonlinear vibration analysis of FGM sandwich structure under linear and nonlinear temperature distributions numerically using the higher-order shear deformation theory (HSDT). A parametric study on the buckling behavior of a sandwich beam consisting of a porous ceramic core including the effects of length-to-thickness ratio, the volume fraction of FGM, and various porosity patterns based on third-order shear deformation theory (TSDT) was presented by Derikvand et al. [19]. The governing equilibrium equations were solved for different end conditions using the differential transform method and the physical neutral axis of the beam. Li et al. [20] used hyperbolic tangent shear deformation theory for the analysis of free vibration of FG honeycomb sandwich plates with negative Poisson's ratio. They solved the derived governing dynamic equations by applying Navier's method and fluid-solid interface conditions. The corresponding results display that the FG honeycomb core with negative Poisson's ratio can yield much lower frequencies. Instability analysis of axially moving sandwich plates with magnetorheological core and polymeric face sheets reinforced with graphene nanoplatelets by using FSDT was studied by Ghorbanpour Arani et al. [21]. The Halpin–Tsai model and the rule of mixture are utilized to estimate the effective mechanical properties. A novel unified model for vibration analysis of a thick-section sandwich structure was presented based on the variational asymptotic method by Li et al. [22]. They studied the effects of temperature gradients in the thickness direction, core thickness, and boundary conditions by a detailed parametric study. Liu et al. [23] analyzed the buckling and vibration studies of the sandwich plates based on the isogeometric analysis in conjunction with the refined shear deformation theory.

Many researchers have studied the mechanical behavior of structures over the past centuries. Today, with the advancement of technology and the development of industries, achieving the exact results requires the use of new models and methods. Laminated structures are used in many engineering industries. The different theories are used to simulate and obtain analytical results the most common of these theories are Classical plate theory (CPT), FSDT, and HSDT. As the thickness of the sheet increases, the accuracy of these theories decreases. Size effects play a significant role in predicting mechanical behavior when the structure is being studied on a small scale. The best alternative approach to studying the mechanical behavior of materials is the use of the continuum mechanics

relationships. The effect of size is not taken into account in classical continuum mechanics theory. For this reason, this theory cannot predict the mechanical behavior of nanostructures and microstructures well. Various theories including Strain gradient theory (SGT), Modified strain gradient theory (MSGT), Couple stress theory (CST), and Modified couple stress theory (MCST), are proposed to eliminate this defect. Layer-wise (LW) and zig-zag (ZZ) theories provide sufficiently accurate responses for relatively thick laminated structures. These theories can capture the inter-laminar stress fields near the edges. Refined plate theories (RPT) are theories that assume the uniaxial and lateral displacements have bending and shear components. In them, the bending and shear components do not contribute toward shear forces and bending moments, respectively. The most interesting feature of these theories is that they have high accuracy for a quadratic variation of the transverse shear strains across the thickness and also satisfies the zero traction boundary conditions on the top and bottom surfaces of the plate without using shear correction factors. Several models of RPT with different form functions by dividing the transverse displacement into bending and shear parts for plate structures are proposed. Quasi-three-dimensional and Three-dimensional (3D) are the new contributions of the proposed theories which are compatible with the numerical method and naturally taken into account in the thickness direction. Examples of the use of these theories in the published articles are expressed as follows.

Ren et al. [24] derived the nonlocal strong forms for various physical models in traditional methods. They derived the nonlocal forms of electro-magneto-elasticity thin plate and phase-field fracture method based on the nonlocal operator method by using the variational principle/weighted residual method. Pham et al. [25] studied the nonlocal dynamic response of sandwich nanoplates with a porous FG core using higher-order isogeometric theory. They extracted the governing equations of motion of sandwich nanoplates by the Hamilton principle and solved them by the Newmark method. Dynamic instability behavior of graphene nanoplatelets-reinforced porous sandwich plates subjected to periodic in-plane compressive loads based on a four-variable refined quasi-3D plate theory was investigated by Nguyen and Phan [26]. They used Bolotin's method to solve the Mathieu–Hill equation. Their results show that the thickness stretching effect should be carefully evaluated for moderate to thick plate structures, such as sandwich plates. Free vibration and buckling analyses of piezoelectric–piezomagnetic FG microplates in the thermal environment using MSGT were investigated by Hung et al. [27]. They derived the equilibrium equations by using Hamilton's principle. They reported the effect of the electric voltage, power index, magnetic potential, length scale parameters, and geometrical parameters on the dimensionless frequencies and critical buckling loads of microplates. Jin [28] used a refined plate theory to examine the Interlaminar stress analysis of composite laminated plates reinforced with FG graphene particles. Tharwan et al. [29] utilized a novel refined three-variable quasi-3D shear deformation theory to study the buckling behavior of multi-directional FG curved nanobeam rested on an elastic foundation. They used a novel solution to effectively address a range of boundary conditions. Quasi 3D free vibration and buckling analysis of non-uniform thickness sandwich porous plates in a hygro-thermal environment utilizing a refined plate theory and novel finite element model were provided by Hai Van and Hong [30]. They considered the non-uniform thickness sandwich porous plates as bi-directional FGM. Their results reveal that the novel porosity patterns and the boundary conditions have a substantial impact on the mechanical behaviors of sandwich porous plates. Shahmohammadi et al. [31] extended the modified nonlocal FSDT to study buckling analysis of multilayered composite plates reinforced with FG carbon nanotube or FG graphene platelets resting on elastic foundations. A novel quasi-3D hyperbolic HSDT in association with nonlocal MSGD was considered by Ghandourah et al. [32] to analyze the bending and buckling behaviors of FG graphene-reinforced nanocomposite plates. The modified model of Halpin–Tsai and the rule of mixture were employed to compute the effective Young's modulus, Poisson's ratio, and mass density of FG graphene-reinforced nanocomposite plates. The inclusion of thickness stretching, nonlocal parameters, and length-scale parameters has a significant effect on the response of the GRNC plate. Hung et al. [33] employed a quasi-3D HSDT to study the bending response of FG-saturated porous nanoplate resting on an elastic foundation. According to their findings, the deflection and stresses increase by increasing the values of the nonlocal parameter. Daikh et al. [34] proposed a Quasi-3D HSDT to examine the buckling behavior of bilayer FG porous plates based on nonlocal strain gradient theory (NSGT). They developed the equilibrium equations using the virtual work principle and solved them utilizing the Galerkin method to cover various boundary conditions. Shahzad et al. [35] analyzed the size-dependent nonlinear dynamic of piezoelectric nanobeam subjected to a time-dependent mechanical uniform load. They formulated the NSGT based on a quasi-3D beam theory to take into account the size dependency.

Sandwich structures are one of the most advanced and modern structures that are utilized for strengthening based on the materials used in their construction. Fixed and mobile refrigerated warehouses, metal industries, spatial structures, and industrial and semi-industrial cold stores are examples of the use of sandwich structures in different industries. Piezoelectric materials have been widely employed as sensors and actuators in microelectromechanical systems (MEMS) and nanoelectromechanical systems (NEMS). In addition, various piezoelectric materials have

been considered for applications in energy harvesting, biomedical engineering, and additive manufacturing. Therefore, due to the existence of piezoelectric layers, piezoelectric nano-sandwiches have many applications in the medical industries including drug delivery, cartilage, nerve, skin, tendon, and muscle regeneration as well as military industries.

Many researchers have investigated the behavior of structures over the past centuries. Today, based on the growth and development of industries and the increasing progress of technology, it is necessary to achieve accurate and reliable results using new models and methods. The use of piezoelectric face sheets as sensors and actuators as well as protection and prevention of damage to FGMs is of great importance considering the cost of construction and the production process of these materials. According to the comprehensive literature survey and the best of the authors' knowledge, there has been no attempt concerning the study of the bi-axial buckling analysis of FG nano-plate covered with piezoelectric face-sheets by considering elastic foundations. Motivated by these considerations, the current paper is the first attempt to present the exact solution for size-dependent quasi-3D buckling analysis of a three-layer FG nanoplate integrated with piezoelectric layers supported by orthotropic Pasternak medium subjected to electric field and in-plane forces. The surface effect responsible for size-dependent characteristics can become distinctly important for piezoelectric nanomaterials in which large surface-to-volume ratio. Also, understanding the buckling behavior of sandwich nano-systems could be a key point for the application in electromechanical resonators, hence, for the first time surface effect, neutral surface position of FGMs and thickness stretching effects together with NSGT are applied to sandwich piezoelectric nanoplate. Eventually, one of the innovations of the presented research is the presentation of comparative results in different models for the critical buckling load of the nano-plate.

2 THEORETICAL FORMULATIONS

2.1 Basic Assumptions

The following assumptions based on the equations of the quasi-three-dimensional theory are presented in this paper to accurately simulate the behavior of the desired sandwich structure with a close approximation of the actual material properties. This theory reliably approximates the actual behavior of thick plates in the thickness direction, considering that σ_3 is significantly smaller compared to τ_{13} and τ_{23}, except at the edges of the structure. The assumptions underlying the current theory and the used materials are outlined as follows:

- It is assumed that there are no slip conditions between the core and the face sheets, ensuring complete continuity and integration between all layers.
- The FGM is modeled as a linear elastic material in the pre-yield condition.
- The origin of the Cartesian coordinate system is placed at the neutral surface of the FG plate.
- The displacements are relatively small compared to the plate thickness, leading to infinitesimal strains.
- The displacements U in the x-direction and V in the y-direction are composed of extension, bending, and shear components.
- The transverse displacement w comprises three parts: bending (w_b) and shear (w_s) and normal stress (ϕ) (stretching effect). These components are solely functions of the coordinates x, y, z and time (t).

2.2 Theoretical Formulations

Consider a rectangular sandwich nanoplate with FGM core and piezoelectric face-sheets at the top and bottom of the core via length a, width b, and total thickness h according to Fig. 1. The thickness of the core and bonded layers are h_c and h_p, respectively. The displacement field of the current formulation is obtained based on the above assumptions. In this research, a higher-order quasi-3D theory according to the four-variable plate theory is developed by considering the thickness stretching parameter. Based on the given assumptions, the considered displacement field is capable of satisfying the transverse shear stresses related to shear strains at the uppermost and lowermost surfaces of the sandwich structure. Hence, the displacement field at any point of the three-layered nanoplate can be expressed as below [35,36];

$$U(x, y, z_{ns}, t) = u_0 + u_b + u_s \tag{1}$$

$$V(x, y, z_{ns}, t) = v_0 + v_b + v_s \tag{2}$$

$$W(x, y, z_{ns}, t) = w_b + w_s + g(z_{ns})\varphi(x, y, t) \tag{3}$$

The bending components u_b and v_b are considered analogous to the displacements described by classical plate theory. Hence, the expressions for u_b and v_b can be formulated as follows [25,37]:

$$u_b = -z_{ns}\frac{\partial w_b}{\partial x} \qquad\qquad v_b = -z_{ns}\frac{\partial w_b}{\partial y} \tag{4}$$
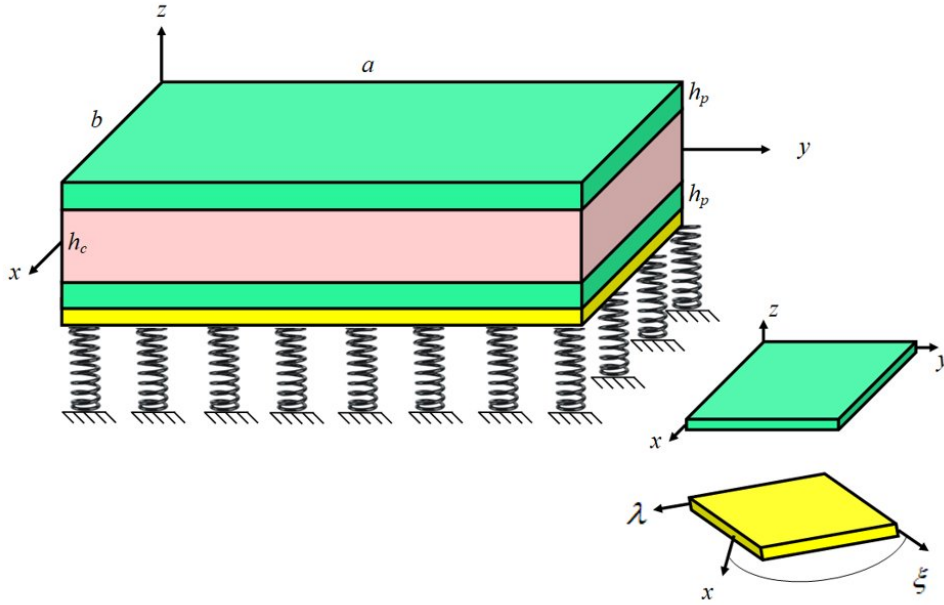
Fig. 1
Geometry of three-layered FG nano-plate integrated with piezoelectric face-sheets.

The shear components u_s and v_s together with w_s create parabolic variations in shear strains γ_{xz} and γ_{yz}. This, in turn, affects the shear stresses τ_{xz} and τ_{yz} throughout the plate's thickness, ensuring that τ_{xz} and τ_{yz} are zero at the top and bottom faces of the plate. As a result, the expressions for u_s and v_s can be defined as follows [26,37,38]:

$$u_s = -f(z_{ns})\frac{\partial w_s}{\partial x} \qquad\qquad v_s = -f(z_{ns})\frac{\partial w_s}{\partial y} \tag{5}$$

On the other hand, u_0 and v_0 represent the displacements in the x and y directions at a corresponding point on the reference surface and also w_b and w_s are the bending and shear components of the transverse displacement, respectively. $f(z_{ns})$ represents a shape function that estimates the distribution of shear stress across the plate's thickness, eliminating the need for any shear correction factor. This shape function can originate from different types of functions, including trigonometric, polynomial, and hyperbolic forms. A polynomial function is selected in this study, similar to the utilized methodology in the hybrid-type quasi-3D shear deformation theory. The shape functions $f(z_{ns})$ and $g(z_{ns})$ can be expressed as [26,39];

$$f(z_{ns}) = z_{ns}\left[-\frac{1}{4} + \frac{5}{3}\left(\frac{z_{ns} + z_0}{h}\right)^2\right]$$

(6)

$$g(z_{ns}) = 1 - f'(z_{ns})$$

(7)

The linear strain-displacement relations based on the quasi-3D displacement field can be written as:

$$\varepsilon_{xx} = \varepsilon_{xx0} + z_{ns}\kappa_{xx}^b + f(z_{ns})\kappa_{xx}^s, \qquad \varepsilon_{yy} = \varepsilon_{yy0} + z_{ns}\kappa_{yy}^b + f(z_{ns})\kappa_{yy}^s, \qquad \varepsilon_{zz} = g'(z_{ns})\varphi_{zz}$$

$$\gamma_{xy} = \varepsilon_{xy0} + z_{ns}\kappa_{xy}^b + f(z_{ns})\kappa_{xy}^s, \qquad \gamma_{xz} = g(z_{ns})\kappa_{xz}^s, \qquad \gamma_{yz} = g(z_{ns})\kappa_{yz}^s$$

(8)

$$\varepsilon_{xx0} = \frac{\partial u_0}{\partial x}, \qquad \varepsilon_{yy0} = \frac{\partial v_0}{\partial y}, \qquad \varepsilon_{xy0} = \frac{\partial v_0}{\partial x} + \frac{\partial u_0}{\partial y}$$

$$\kappa_{xx}^b = -\frac{\partial^2 w_b}{\partial x^2}, \qquad \kappa_{yy}^b = -\frac{\partial^2 w_b}{\partial y^2}, \qquad \kappa_{xy}^b = -2\frac{\partial^2 w_b}{\partial y \partial x}$$

$$\kappa_{xx}^s = -\frac{\partial^2 w_s}{\partial x^2}, \qquad \kappa_{yy}^s = -\frac{\partial^2 w_s}{\partial y^2}, \qquad \kappa_{xy}^s = -2\frac{\partial^2 w_s}{\partial y \partial x}$$

$$\kappa_{xz}^s = \frac{\partial w_s}{\partial x} + \frac{\partial \varphi}{\partial x}, \qquad \kappa_{yz}^s = \frac{\partial w_s}{\partial y} + \frac{\partial \varphi}{\partial y}$$

(9)

2.3 Piezoelectric Materials

Piezoelectric materials have the unique capacity to regulate electrical phases. These materials can produce various physical and chemical responses to electrical phase changes, such as pressure or electric fields. Their key features include high precision and sensitivity, stability and durability, and rapid response times. These distinctive capabilities play an essential role in advancing modern technologies. With the advancement of nanotechnology and composite materials, the applications of piezoelectric materials are expected to expand into new domains, driving the development of more intelligent devices and systems. The constitutive piezo-elasticity relations for a piezoelectric material based on the continuum mechanics approach can be formulated using stress and strain components, electric displacement relations, and the field strength matrix as follows [40]:

$$\begin{Bmatrix} \sigma_{xx}^p \\ \sigma_{yy}^p \\ \sigma_{zz}^p \\ \tau_{yz}^p \\ \tau_{xz}^p \\ \tau_{xy}^p \end{Bmatrix} = \begin{bmatrix} C_{11}^p & C_{12}^p & C_{13}^p & 0 & 0 & 0 \\ C_{12}^p & C_{22}^p & C_{23}^p & 0 & 0 & 0 \\ C_{13}^p & C_{23}^p & C_{33}^p & 0 & 0 & 0 \\ 0 & 0 & 0 & C_{44}^p & 0 & 0 \\ 0 & 0 & 0 & 0 & C_{55}^p & 0 \\ 0 & 0 & 0 & 0 & 0 & C_{66}^p \end{bmatrix} \begin{Bmatrix} \varepsilon_{xx} \\ \varepsilon_{yy} \\ \varepsilon_{zz} \\ \gamma_{yz} \\ \gamma_{xz} \\ \gamma_{xy} \end{Bmatrix} - \begin{bmatrix} 0 & 0 & e_{31}^p \\ 0 & 0 & e_{32}^p \\ 0 & 0 & e_{33}^p \\ 0 & e_{24}^p & 0 \\ e_{15}^p & 0 & 0 \\ 0 & 0 & 0 \end{bmatrix} \begin{Bmatrix} E_x \\ E_y \\ E_z \end{Bmatrix}$$

(10)

$$\begin{Bmatrix} D_x \\ D_y \\ D_z \end{Bmatrix} = \begin{bmatrix} 0 & 0 & 0 & 0 & e_{15}^p & 0 \\ 0 & 0 & 0 & e_{24}^p & 0 & 0 \\ e_{31}^p & e_{32}^p & e_{33}^p & 0 & 0 & 0 \end{bmatrix} \begin{Bmatrix} \varepsilon_{xx} \\ \varepsilon_{yy} \\ \varepsilon_{zz} \\ \gamma_{yz} \\ \gamma_{xz} \\ \gamma_{xy} \end{Bmatrix} + \begin{bmatrix} \epsilon_{11}^p & 0 & 0 \\ 0 & \epsilon_{22}^p & 0 \\ 0 & 0 & \epsilon_{33}^p \end{bmatrix} \begin{Bmatrix} E_x \\ E_y \\ E_z \end{Bmatrix}$$

(11)

in which C_{ij}^p are stiffness matrix components, e_{ij}^p are piezo-electric coefficients, and ϵ_{ii}^p are dielectric permeability coefficients. D_i represent electric displacements and E_i are electric field components. The electric fields must be chosen to satisfy Maxwell's relation and can be represented as follows [40-41]:

$$E_i = -\nabla \Phi(x,y,z,t) \tag{12}$$

$$\Phi(x,y,z,t) = 2(\frac{\tilde{z}V_0}{h_p}) - \cos(\frac{\pi\tilde{z}}{h_p})\phi(x,y,t) \tag{13}$$

where V_0 represents the externally applied electric voltage between the top and bottom of the piezoelectric layers. Additionally, $\phi(x,y,t)$ denotes the spatial variation of the electric potential in two-dimensional directions. Consequently, the electric components in the three spatial directions are as follow [38,41]:

$$E_x = -\frac{\partial}{\partial x}\Phi(x,y,z,t) = \cos(\pi\tilde{z}/h_p)\frac{\partial}{\partial x}\phi(x,y,t) \tag{14}$$

$$E_y = -\frac{\partial}{\partial y}\Phi(x,y,z,t) = \cos(\pi\tilde{z}/h_p)\frac{\partial}{\partial y}\phi(x,y,t) \tag{15}$$

$$E_z = -\frac{\partial}{\partial \tilde{z}}\Phi(x,y,z,t) = -2(\frac{V_0}{h_p}) - (\frac{\pi}{h_p})\sin(\frac{\pi\tilde{z}}{h_p})\phi(x,y,t) \tag{16}$$

The transformed coordinates for the upper and lower layers, relative to the mid-plane of the piezoelectric face-sheets can be expressed as follows.

$$\tilde{z} = z - \frac{h_c}{2} - \frac{h_p}{2} \tag{17}$$

$$\tilde{z} = z + \frac{h_c}{2} + \frac{h_p}{2} \tag{18}$$

2.4 FGM Properties

FGMs are smart materials typically composed of ceramic and metal and the effective properties of these materials continuously vary along the thickness direction according to the specific relationship. In this paper, the material properties of the FG plate change based on the power-law distribution. Hence, the effective non-homogeneous properties of FG nanoplate utilizing the rule of mixture can be expressed by [40-44]:

$$P(z) = P_M + (P_C - P_M)\left(\frac{1}{2} + \frac{z}{h}\right)^k \tag{19}$$

In this Eq., subscripts C and M represent the properties of ceramic and metallic materials, respectively. Additionally, the parameter k indicates the gradient index distribution of properties along the thickness direction of the plate. Due to the asymmetric distribution of properties along the functional grading of these materials, the position of the neutral surface does not coincide with the mid-plane in the graded direction. The inherent asymmetry in material properties of FG plates relative to the mid-plane causes the stretching and bending equations to be coupled. Thus, by appropriately selecting the origin of the coordinates in the direction of property variations, the coupling between stretching and bending can be neglected. The symmetry of properties along the direction of variation significantly simplifies the analysis of these materials. Hence, two different planes z_{ms} and z_{ns} are considered for the measurement of z from the middle surface and the neutral surface of the plate, respectively, to specify the position of the neutral surface of FG plates, as shown in Fig. 2.

$$V_C = \left(\frac{1}{2} + \frac{z_{ms}}{h_c}\right)^k = \left(\frac{1}{2} + \frac{z_{ns} + z_0}{h_c}\right)^k \tag{20}$$

$$E(z) = E_M + E_{CM}V_C, \qquad \rho(z) = \rho_M + \rho_{CM}V_C \tag{21}$$

$$E_{CM} = E_C - E_M, \qquad \rho_{CM} = \rho_C - \rho_M \tag{22}$$

Notably, the material properties at the top and bottom surfaces of the FG plate are pure ceramic and pure metal, respectively. E, ρ are Young's modulus and mass density of FG nanoplate that are assumed to vary according to a power law distribution in terms of the volume fractions of the constituents.
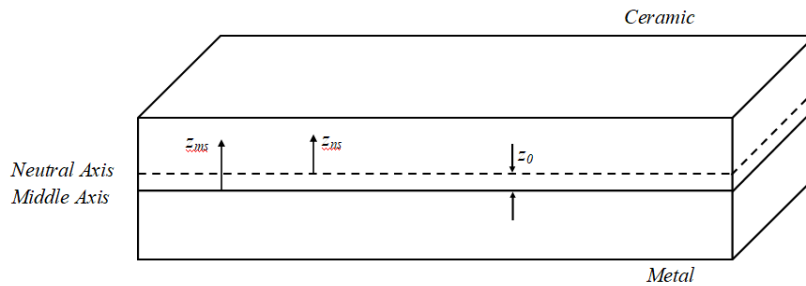
Fig. 2
Neutral surface position of FG nano-plate.

The distance of the neutral surface from the mid-plane is represented by z_0 in Eq. (2) and this distance can be defined as follows [42]:

$$z_0 = \frac{\left(\displaystyle\int_{-h_c/2}^{h_c/2} E(z_{ms}) z_{ms} dz_{ms}\right)}{\left(\displaystyle\int_{-h_c/2}^{h_c/2} E(z_{ms}) dz_{ms}\right)} \tag{23}$$

The linear constitutive relations of a FG plate can be written as [40]:

$$\begin{Bmatrix} \sigma_{xx}^c \\ \sigma_{yy}^c \\ \sigma_{zz}^c \\ \tau_{yz}^c \\ \tau_{xz}^c \\ \tau_{xy}^c \end{Bmatrix} = \begin{bmatrix} Q_{11}^c & Q_{12}^c & Q_{13}^c & 0 & 0 & 0 \\ Q_{12}^c & Q_{22}^c & Q_{23}^c & 0 & 0 & 0 \\ Q_{13}^c & Q_{23}^c & Q_{33}^c & 0 & 0 & 0 \\ 0 & 0 & 0 & Q_{44}^c & 0 & 0 \\ 0 & 0 & 0 & 0 & Q_{55}^c & 0 \\ 0 & 0 & 0 & 0 & 0 & Q_{66}^c \end{bmatrix} \begin{Bmatrix} \varepsilon_{xx} \\ \varepsilon_{yy} \\ \varepsilon_{zz} \\ \gamma_{yz} \\ \gamma_{xz} \\ \gamma_{xy} \end{Bmatrix} \tag{24}$$

Using the material properties defined in Eq. (3), stiffness coefficients, Q_{cij} can be expressed as [40]:

$$Q_{11}^c = Q_{22}^c = Q_{33}^c = \frac{(1-\upsilon)E(z_{nz})}{(1-2\upsilon)(1+\upsilon)}, \qquad Q_{12}^c = Q_{13}^c = Q_{23}^c = \upsilon Q_{11}^c, \qquad Q_{44}^c = Q_{55}^c = Q_{66}^c = \frac{E(z_{nz})}{2(1+\upsilon)} \tag{25}$$

2. ⸱ Non-local Strain Gradient Theory

In this paper, the NSGT is employed to analyze the size-dependent behavior of sandwich nanoplate. A new non-conventional continuum theory of elasticity called NSGT is introduced to simultaneously consider the opposite characteristics of small-scale effects. In this theory, the coupled physical influences of nonlocal and strain gradient size effects are simultaneously considered. By ignoring the effect of body force, the general constitutive relations with the framework of NSGT are written as [45-51]:

$$(1-\mu^2\nabla^2)\{\sigma_{ij}\} = (1-\ell^2\nabla^2)\{C_{ijkl}\varepsilon_{kl} - e_{kij}E_k\} \tag{26}$$

$$(1-\mu^2\nabla^2)\{D_i\} = (1-\ell^2\nabla^2)\{e_{ikl}\varepsilon_{kl} + \kappa_{kij}E_k\} \tag{27}$$

$$\nabla^2 = \partial^2/\partial x^2 + \partial^2/\partial y^2 \tag{28}$$

in which ℓ represents the internal material length scale parameter, μ denotes the nonlocal parameter, and ∇^2 is the Laplacian operator.

2.6 Surface Piezoelectricity Effects

In nano-scale structures, the energy fraction stored in the surface layers is considerably higher than that in the bulk material, and surface or near-surface atoms are typically subject to a range of environmental influences distinct from those affecting bulk atoms. Indeed, a key characteristic of nanostructures is their high surface-to-volume ratio. Consequently, surface elasticity theory is combined with non-classical continuum theory to examine these significant effects. The primary equations for stresses and electric displacements on the surface of piezoelectric materials based on NSGT can be formulated as [49-51]:

$$(1-\mu^2\nabla^2)\{\sigma_{sij}\} = (1-\ell^2\nabla^2)\{C_{sijkl}\varepsilon_{kl} - e_{skij}E_k + \tau_s \aleph\} \tag{29}$$

$$(1-\mu^2\nabla^2)\{D_i\} = (1-\ell^2\nabla^2)\{e_{sikl}\varepsilon_{kl} + \kappa_{skij}E_k\} \tag{30}$$

where $C_{sij}, e_{sij}, \kappa_{sij}$ and τ_s are the surface elastic constants, surface piezoelectric constants, surface dielectric constants, and the residual surface stress tensor. Also, $\aleph = \{\partial(w_s + w_b)/\partial y, \partial(w_s + w_b)/\partial x\}$.

2. ⸱ Equations of motion

The equilibrium governing equations for the nonlocal sandwich FG nanoplate are formulated using Hamilton's principle. According to the Hamilton's principle, one can get that [52-56];

$$\int_0^t (\delta U - \delta W)dt = 0 \tag{31}$$

where δU and δW are the first variation of strain energy and work done by external forces leading foundation and applied electrical field, respectively. The total potential energy of sandwich nanoplate with FG core and piezoelectric face sheets including both the bulk part and two surface layers can be expressed as [54]:

$$U = \frac{1}{2}\int_A \int_{-h/2}^{h/2}(\sigma_{ij}^b \varepsilon_{ij} - D_i^b E_i)dzdA + \frac{1}{2}\int_{S^+}(\sigma_{ij}^p \varepsilon_{ij} - D_i^p E_i)dS^+ + \frac{1}{2}\int_{S^-}(\sigma_{ij}^p \varepsilon_{ij} - D_i^p E_i)dS^- \tag{32}$$

where S^+ and S^- relates to upper surface layers and lower surface layers, respectively.

$$U = \frac{1}{2}\int_A \begin{pmatrix} \frac{\partial u}{\partial x}N_x + \frac{\partial u}{\partial y}N_{xy} + \frac{\partial v}{\partial y}N_y + \frac{\partial v}{\partial x}N_{xy} - \frac{\partial^2 w_b}{\partial x^2}M_{bx} - \frac{\partial^2 w_b}{\partial y^2}M_{by} - 2\frac{\partial^2 w_b}{\partial x\partial y}M_{bxy} \\ -2\frac{\partial^2 w_s}{\partial x\partial y}M_{sxy} - \frac{\partial^2 w_s}{\partial x^2}M_{sx} - \frac{\partial^2 w_s}{\partial y^2}M_{sy} + N_z\varphi + \frac{\partial(w_s-\varphi)}{\partial x}Q_{xz} + \frac{\partial(w_s-\varphi)}{\partial y}Q_{yz} \end{pmatrix}dA$$

$$+\frac{1}{2}\int_A \int_{h_c/2-z_0}^{h_c/2+h_p-z_0}\left((D_x^b+D_x^s)\cos\left(\frac{\pi\bar{z}_{ns}}{h_p}\right)\frac{\partial\phi}{\partial x} + (D_y^b+D_y^s)\cos\left(\frac{\pi\bar{z}_{ns}}{h_p}\right)\frac{\partial\phi}{\partial y} + \frac{(D_z^b+D_z^s)\pi}{h_p}\sin\left(\frac{\pi\bar{z}_{ns}}{h_p}\right)\phi\right)dzdA \tag{33}$$

$$+\frac{1}{2}\int_A \int_{-h_c/2-h_p-z_0}^{-h_c/2-z_0}\left((D_x^b+D_x^s)\cos\left(\frac{\pi\bar{z}_{ns}}{h_p}\right)\frac{\partial\phi}{\partial x} + (D_y^b+D_y^s)\cos\left(\frac{\pi\bar{z}_{ns}}{h_p}\right)\frac{\partial\phi}{\partial y} + \frac{(D_z^b+D_z^s)\pi}{h_p}\sin\left(\frac{\pi\bar{z}_{ns}}{h_p}\right)\phi\right)dzdA$$

The converted coordinate based on the neutral axis is $\bar{z}_{ns} = z_{ns} \pm (h_c/2) \pm (h_p/2) - z_0$. The above equation, N, M and Q implies the force, moment and transverse shear stress resultants that can be described as:

$$\begin{bmatrix} N_x \\ N_y \\ N_{xy} \end{bmatrix} = \left(\int_{-h_c/2-h_p-z_0}^{-h_c/2-z_0}\begin{bmatrix}\sigma_{xx}^p\\\sigma_{yy}^p\\\sigma_{xy}^p\end{bmatrix}dz + \begin{bmatrix}\sigma_{xx}^p\\\sigma_{yy}^p\\\sigma_{xy}^p\end{bmatrix}_{-h_c/2-z_0} + \begin{bmatrix}\sigma_{xx}^p\\\sigma_{yy}^p\\\sigma_{xy}^p\end{bmatrix}_{-h_c/2-h_p-z_0}\right) + \left(\int_{-h_c/2-z_0}^{h_c/2-z_0}\begin{bmatrix}\sigma_{xx}^c\\\sigma_{yy}^c\\\sigma_{xy}^c\end{bmatrix}dz\right)$$

$$+\left(\int_{h_c/2-z_0}^{h_c/2+h_p-z_0}\begin{bmatrix}\sigma_{xx}^p\\\sigma_{yy}^p\\\sigma_{xy}^p\end{bmatrix}dz + \begin{bmatrix}\sigma_{xx}^p\\\sigma_{yy}^p\\\sigma_{xy}^p\end{bmatrix}_{h_c/2-z_0} + \begin{bmatrix}\sigma_{xx}^p\\\sigma_{yy}^p\\\sigma_{xy}^p\end{bmatrix}_{h_c/2+h_p-z_0}\right) \tag{34}$$

$$\begin{bmatrix} M_{bx} \\ M_{by} \\ M_{bxy} \end{bmatrix} = \left(\int_{-h_c/2-h_p-z_0}^{-h_c/2-z_0}\begin{bmatrix}\sigma_{xx}^p\\\sigma_{yy}^p\\\sigma_{xy}^p\end{bmatrix}zdz + z\begin{bmatrix}\sigma_{xx}^p\\\sigma_{yy}^p\\\sigma_{xy}^p\end{bmatrix}_{-h_c/2-z_0} + z\begin{bmatrix}\sigma_{xx}^p\\\sigma_{yy}^p\\\sigma_{xy}^p\end{bmatrix}_{-h_c/2-h_p-z_0}\right) + \left(\int_{-h_c/2-z_0}^{h_c/2-z_0}\begin{bmatrix}\sigma_{xx}^c\\\sigma_{yy}^c\\\sigma_{xy}^c\end{bmatrix}zdz\right)$$

$$+\left(\int_{h_c/2-z_0}^{h_c/2+h_p-z_0}\begin{bmatrix}\sigma_{xx}^p\\\sigma_{yy}^p\\\sigma_{xy}^p\end{bmatrix}z\,dz + z\begin{bmatrix}\sigma_{xx}^p\\\sigma_{yy}^p\\\sigma_{xy}^p\end{bmatrix}_{h_c/2-z_0} + z\begin{bmatrix}\sigma_{xx}^p\\\sigma_{yy}^p\\\sigma_{xy}^p\end{bmatrix}_{h_c/2+h_p-z_0}\right) \tag{35}$$

$$\begin{bmatrix} M_{sx} \\ M_{sy} \\ M_{sxy} \end{bmatrix} = \left(\int_{-h_c/2-h_p-z_0}^{-h_c/2-z_0}\begin{bmatrix}\sigma_{xx}^p\\\sigma_{yy}^p\\\sigma_{xy}^p\end{bmatrix}f(z_{ns})dz + f(z_{ns})\begin{bmatrix}\sigma_{xx}^p\\\sigma_{yy}^p\\\sigma_{xy}^p\end{bmatrix}_{-h_c/2-z_0} + f(z_{ns})\begin{bmatrix}\sigma_{xx}^p\\\sigma_{yy}^p\\\sigma_{xy}^p\end{bmatrix}_{-h_c/2-h_p-z_0}\right) + \left(\int_{-h_c/2-z_0}^{h_c/2-z_0}\begin{bmatrix}\sigma_{xx}^c\\\sigma_{yy}^c\\\sigma_{xy}^c\end{bmatrix}f(z_{ns})dz\right)$$

$$+\left(\int_{h_c/2-z_0}^{h_c/2+h_p-z_0}\begin{bmatrix}\sigma_{xx}^p\\\sigma_{yy}^p\\\sigma_{xy}^p\end{bmatrix}f(z_{ns})dz + f(z_{ns})\begin{bmatrix}\sigma_{xx}^p\\\sigma_{yy}^p\\\sigma_{xy}^p\end{bmatrix}_{h_c/2-z_0} + f(z_{ns})\begin{bmatrix}\sigma_{xx}^p\\\sigma_{yy}^p\\\sigma_{xy}^p\end{bmatrix}_{h_c/2+h_p-z_0}\right) \tag{36}$$

$$\begin{bmatrix} Q_{xz} \\ Q_{yz} \end{bmatrix} = \left(\int_{-h_c/2-h_p-z_0}^{-h_c/2-z_0} \begin{bmatrix} \sigma_{xz}^p \\ \sigma_{yz}^p \end{bmatrix} g(z_{ns})dz + g(z_{ns}) \begin{bmatrix} \sigma_{xz}^p \\ \sigma_{yz}^p \end{bmatrix}\Bigg|_{-h_c/2-z_0} + g(z_{ns}) \begin{bmatrix} \sigma_{xz}^p \\ \sigma_{yz}^p \end{bmatrix}\Bigg|_{-h_c/2-h_p-z_0} \right) + \left(\int_{-h_c/2-z_0}^{h_c/2-z_0} \begin{bmatrix} \sigma_{xz}^c \\ \sigma_{yz}^c \end{bmatrix} g(z_{ns})dz \right)$$
$$+ \left(\int_{h_c/2-z_0}^{h_c/2+h_p-z_0} \begin{bmatrix} \sigma_{xz}^p \\ \sigma_{yz}^p \end{bmatrix} g(z_{ns})dz + g(z_{ns}) \begin{bmatrix} \sigma_{xz}^p \\ \sigma_{yz}^p \end{bmatrix}\Bigg|_{h_c/2-z_0} + g(z_{ns}) \begin{bmatrix} \sigma_{xz}^p \\ \sigma_{yz}^p \end{bmatrix}\Bigg|_{h_c/2+h_p-z_0} \right) \tag{37}$$

$$[N_z] = \left(\int_{-h_c/2-h_p-z_0}^{-h_c/2-z_0} \begin{bmatrix} \sigma_{zz}^p \end{bmatrix} g'(z_{ns})dz + g'(z_{ns}) \begin{bmatrix} \sigma_{zz}^p \end{bmatrix}\Bigg|_{-h_c/2-z_0} + g'(z_{ns}) \begin{bmatrix} \sigma_{zz}^p \end{bmatrix}\Bigg|_{-h_c/2-h_p-z_0} \right) + \left(\int_{-h_c/2-z_0}^{h_c/2-z_0} \begin{bmatrix} \sigma_{zz}^c \end{bmatrix} g'(z_{ns})dz \right)$$
$$+ \left(\int_{h_c/2-z_0}^{h_c/2+h_p-z_0} \begin{bmatrix} \sigma_{zz}^p \end{bmatrix} g'(z_{ns})dz + g'(z_{ns}) \begin{bmatrix} \sigma_{zz}^p \end{bmatrix}\Bigg|_{h_c/2-z_0} + g'(z_{ns}) \begin{bmatrix} \sigma_{zz}^p \end{bmatrix}\Bigg|_{h_c/2+h_p-z_0} \right) \tag{38}$$

The external works can be extracted into two parts. One part is an orthotropic Pasternak medium and the other part is a two-dimensional electric field applied to the piezoelectric face sheets [53, 57-60].

$$W = \iint (\bar{N} - \bar{F})w\, dA \tag{39}$$

In contrast to other models, this foundation can simulate both normal and shear loads in any given direction. The applied force induced by the orthotropic Pasternak foundation can be defined as [57,58]:

$$\bar{F} = K_w w - K_{gx} \left(\cos^2\theta \frac{\partial^2 w}{\partial x^2} + \sin 2\theta \frac{\partial^2 w}{\partial x\partial y} + \sin^2\theta \frac{\partial^2 w}{\partial y^2} \right) - K_{gy} \left(\sin^2\theta \frac{\partial^2 w}{\partial x^2} - \sin 2\theta \frac{\partial^2 w}{\partial x\partial y} + \cos^2\theta \frac{\partial^2 w}{\partial y^2} \right) \tag{40}$$

in which K_w, K_{gx}, K_{gy} describes linear spring coefficient and shear layers in two arbitrary directions, respectively. Also, the angle θ specifies the orientation of the local x-direction of the orthotropic foundation with respect to the global x-axis of the system. The applied forces from the electric field can be calculated as [45,51,60-61]:

$$\bar{N} = \{\bar{N}_{xx} \quad \bar{N}_{yy}\} \left(\frac{\partial^2}{\partial x^2} + \frac{\partial^2}{\partial y^2} \right)(w_b + w_s) \tag{41}$$

In above Eq., longitudinal ($\bar{N}_{xx}$) and transverse ($\bar{N}_{yy}$) resultant are $N_{xx} + N_{ex}$ and $N_{yy} + N_{ey}$, respectively. In this regard N_{xx} and indicates in-plane applied forces exerting on the sandwich nanoplate. On the other hand, N_{ex}, N_{ey} are the electric loading in x-direction and y-direction, respectively. These parameters can be expressed as [52]:

$$N_{ex} = -\int_{h_p} e_{31} \frac{2V_0}{h_p}, \qquad\qquad N_{ey} = -\int_{h_p} e_{32} \frac{2V_0}{h_p} \tag{42}$$

Finally, based on Hamilton's principles, integrating by parts, separating the unknown coefficients, and setting the coefficient of mechanical and electrical $(\delta u, \delta v, \delta w_b, \delta w_s, \delta\varphi, \delta\phi)$ to zero, separately, the nonlocal governing equations of sandwich nanoplate resting on elastic foundation under an electrical field in terms of the displacement can be derived as follows:

$$\delta u : (1-\ell^2\nabla^2) \left\{ \begin{array}{l} (A_{66}^b + A_{66}^s)(\frac{\partial^2 v}{\partial y\partial x} + \frac{\partial^2 u}{\partial y^2}) - (B_{11}^b + B_{11}^s)\frac{\partial^3 w_b}{\partial x^3} - 2(F_{66}^b + F_{66}^s)\frac{\partial^3 w_s}{\partial y^2\partial x} - (F_{11}^b + F_{11}^s)\frac{\partial^3 w_s}{\partial x^3} \\[2mm] -(B_{12}^b + B_{12}^s)\frac{\partial^3 w_b}{\partial y^2\partial x} - (F_{12}^b + F_{12}^s)\frac{\partial^3 w_s}{\partial y^2\partial x} + (D_{11}^b + D_{11}^s + E_{11}^b + E_{11}^s)\frac{\partial\phi}{\partial x} - 2(B_{66}^b + B_{66}^s)\frac{\partial^3 w_b}{\partial y^2\partial x} \\[2mm] + (A_{11}^b + A_{11}^s)\frac{\partial^2 u}{\partial x^2} + (A_{12}^b + A_{12}^s)\frac{\partial^2 v}{\partial y\partial x} \end{array} \right\} = 0 \tag{43}$$

$$\delta v : (1-\ell^2\nabla^2)\begin{Bmatrix}(A_{12}^b+A_{12}^s)\dfrac{\partial^2 u}{\partial y\partial x}-2(B_{66}^b+B_{66}^s)\dfrac{\partial^3 w_b}{\partial y\partial x^2}-(B_{11}^b+B_{11}^s)\dfrac{\partial^3 w_b}{\partial y^3}-(F_{11}^b+F_{11}^s)\dfrac{\partial^3 w_s}{\partial y^3}-(B_{12}^b+B_{12}^s)\dfrac{\partial^3 w_b}{\partial y\partial x^2}\\[2mm] -(F_{12}^b+F_{12}^s)\dfrac{\partial^3 w_s}{\partial y\partial x^2}+(D_{11}^b+D_{11}^s+E_{11}^b+E_{11}^s)\dfrac{\partial\phi}{\partial y}-2(F_{66}^b+F_{66}^s)\dfrac{\partial^3 w_s}{\partial y\partial x^2}+(A_{11}^b+A_{11}^s)\dfrac{\partial^2 v}{\partial y^2}\\[2mm]+(A_{66}^b+A_{66}^s)(\dfrac{\partial^2 v}{\partial x^2}+\dfrac{\partial^2 u}{\partial y\partial x})\end{Bmatrix}=0 \qquad (44)$$

$$\delta w_b : (1-\ell^2\nabla^2)\begin{Bmatrix}(B_{11}^b+B_{11}^s)(\dfrac{\partial^3 u}{\partial x^3}+\dfrac{\partial^3 v}{\partial y^3})+2(B_{66}^b+B_{66}^s)(\dfrac{\partial^3 v}{\partial y\partial x^2}+\dfrac{\partial^3 u}{\partial y^2\partial x})\\[2mm]-(J_{11}^b+J_{11}^s)(\dfrac{\partial^4 w_b}{\partial x^4}+\dfrac{\partial^4 w_b}{\partial y^4})+(D_{22}^b+D_{22}^s+E_{22}^b+E_{22}^s)(\dfrac{\partial^2\phi}{\partial x^2}+\dfrac{\partial^2\phi}{\partial y^2})\\[2mm]+(B_{12}^b+B_{12}^s)(\dfrac{\partial^3 v}{\partial y\partial x^2}+\dfrac{\partial^3 u}{\partial y^2\partial x})-2(R_{12}^b+R_{12}^s-2R_{66}^b-2R_{66}^s)\dfrac{\partial^4 w_s}{\partial y^2\partial x^2}\\[2mm]-(R_{11}^b+R_{11}^s)(\dfrac{\partial^4 w_s}{\partial x^4}+\dfrac{\partial^4 w_s}{\partial y^4})-4(J_{66}^b+J_{66}^s)\dfrac{\partial^4 w_b}{\partial y^2\partial x^2}-2(J_{12}^b+J_{12}^s)\dfrac{\partial^4 w_b}{\partial y^2\partial x^2}\end{Bmatrix}+(1-\mu^2\nabla^2)\{\overline{N}-\overline{F}\}=0 \qquad (45)$$

$$\delta w_s : (1-\ell^2\nabla^2)\begin{Bmatrix}2(F_{66}^b+F_{66}^s)(\dfrac{\partial^3 v}{\partial y\partial x^2}+\dfrac{\partial^3 u}{\partial y^2\partial x})-2(R_{12}^b+R_{12}^s)\dfrac{\partial^4 w_b}{\partial y^2\partial x^2}+P_{11}^s(\dfrac{\partial^2 w_b}{\partial x^2}+\dfrac{\partial^2 w_s}{\partial x^2})\\[2mm]-2(L_{12}^b+L_{12}^s)\dfrac{\partial^4 w_s}{\partial y^2\partial x^2}-(R_{11}^b+R_{11}^s)(\dfrac{\partial^4 w_b}{\partial x^4}+\dfrac{\partial^4 w_b}{\partial y^4})+G_{22}^b(\dfrac{\partial^2\varphi}{\partial x^2}+\dfrac{\partial^2 w_s}{\partial x^2})\\[2mm]-(L_{11}^b+L_{11}^s)(\dfrac{\partial^4 w_s}{\partial y^4}+\dfrac{\partial^4 w_s}{\partial x^4})-4(L_{66}^b+L_{66}^s)\dfrac{\partial^4 w_s}{\partial y^2\partial x^2}-4(R_{66}^b+R_{66}^s)\dfrac{\partial^4 w_b}{\partial y^2\partial x^2}\\[2mm]+(F_{12}^b+F_{12}^s)(\dfrac{\partial^3 v}{\partial y\partial x^2}+\dfrac{\partial^3 u}{\partial y^2\partial x})+P_{11}^s(\dfrac{\partial^2 w_b}{\partial y^2}+\dfrac{\partial^2 w_s}{\partial y^2})-H_{11}^b(\dfrac{\partial^2\phi}{\partial x^2}-\dfrac{\partial^2\phi}{\partial y^2})\\[2mm]+(D_{33}^b+D_{33}^s)(\dfrac{\partial^2\varphi}{\partial x^2}+\dfrac{\partial^2\varphi}{\partial y^2})+(E_{33}^b+E_{33}^s)(\dfrac{\partial^2\phi}{\partial x^2}+\dfrac{\partial^2\phi}{\partial y^2})+G_{11}^b(\dfrac{\partial^2\varphi}{\partial y^2}+\dfrac{\partial^2 w_s}{\partial y^2})\\[2mm]+(F_{11}^b+F_{11}^s)(\dfrac{\partial^3 u}{\partial x^3}+\dfrac{\partial^3 v}{\partial y^3})\end{Bmatrix}+(1-\mu^2\nabla^2)\{\overline{N}-\overline{F}\}=0 \qquad (46)$$

$$\delta\varphi : (1-\ell^2\nabla^2)\begin{Bmatrix}(D_{22}^b+D_{22}^s)(\dfrac{\partial^2 w_b}{\partial x^2}+\dfrac{\partial^2 w_b}{\partial y^2})-(D_{11}^b+D_{11}^s)(\dfrac{\partial u}{\partial x}+\dfrac{\partial v}{\partial y})-H_{11}^b(\dfrac{\partial^2\phi}{\partial x^2}-\dfrac{\partial^2\phi}{\partial y^2})+P_{11}^s(\dfrac{\partial^2 w_b}{\partial y^2}+\dfrac{\partial^2 w_s}{\partial y^2})+\\[2mm]G_{11}^b(\dfrac{\partial^2\varphi}{\partial y^2}+\dfrac{\partial^2 w_s}{\partial y^2})+G_{22}^b(\dfrac{\partial^2\varphi}{\partial x^2}+\dfrac{\partial^2 w_s}{\partial x^2})+P_{11}^s(\dfrac{\partial^2 w_b}{\partial x^2}+\dfrac{\partial^2 w_s}{\partial x^2})+(D_{33}^b+D_{33}^s)(\dfrac{\partial^2 w_s}{\partial x^2}+\dfrac{\partial^2 w_s}{\partial y^2})\end{Bmatrix}=0 \qquad (47)$$

$$\delta\phi : (1-\ell^2\nabla^2)\begin{Bmatrix}(I_{11}^b+I_{11}^s)(\dfrac{\partial^2\phi}{\partial x^2}+\dfrac{\partial^2\phi}{\partial y^2})+(B_{33}^b+B_{33}^s)\varphi-(I_{33}^b+I_{33}^s)\phi-(E_{33}^b+E_{33}^s)(\dfrac{\partial^2 w_s}{\partial x^2}+\dfrac{\partial^2 w_s}{\partial y^2})+\\[2mm](E_{11}^b+E_{11}^s)(\dfrac{\partial u}{\partial x}+\dfrac{\partial v}{\partial y})-(E_{22}^b+E_{22}^s)(\dfrac{\partial^2 w_b}{\partial x^2}+\dfrac{\partial^2 w_b}{\partial y^2})+(H_{11}^b+H_{11}^s)(\dfrac{\partial^2\varphi}{\partial x^2}+\dfrac{\partial^2 w_s}{\partial x^2}+\dfrac{\partial^2\varphi}{\partial y^2}+\dfrac{\partial^2 w_s}{\partial y^2})\end{Bmatrix}=0 \qquad (48)$$

where

$$\begin{Bmatrix}A_{ij}^b & B_{ij}^b & J_{ij}^b\\ F_{ij}^b & R_{ij}^b & L_{ij}^b\end{Bmatrix}=\sum_{r=1}^{3}\int_{h_r-z_0}^{h_{r+1}-z_0}C_{ij}^b\begin{Bmatrix}1 & z_{ns} & z_{ns}^2\\ f(z_{ns}) & z_{ns}f(z_{ns}) & f^2(z_{ns})\end{Bmatrix}dz_{ns}\qquad i,j=1,2,6 \qquad (49)$$

$$\left\{D_{ii}^b, E_{ii}^b\right\} = \sum_{r=1}^{3} \int_{h_r - z_0}^{h_{r+1} - z_0} \left[C_{13}^b g'(z_{ns}), \frac{\pi}{h_p} e_{13}^b \sin\left(\frac{\pi \bar{z}_{ns}}{h_p}\right)\right] \left\{1, z_{ns}, f(z_{ns})\right\} dz_{ns} \quad i = 1,2,3 \tag{50}$$

$$\left\{G_{11}^b, G_{22}^b\right\} = \sum_{r=1}^{3} \int_{h_r - z_0}^{h_{r+1} - z_0} \left[C_{44}^b, C_{55}^b\right] g^2(z_{ns}) dz_{ns} \tag{51}$$

$$\left\{H_{11}^b, H_{22}^b\right\} = \sum_{r=1}^{3} \int_{h_r - z_0}^{h_{r+1} - z_0} \left[e_{15}^b, e_{24}^b\right] g(z_{ns}) \cos\left(\frac{\pi \bar{z}_{ns}}{h_p}\right) dz_{ns} \tag{52}$$

$$\left\{I_{11}^b, I_{22}^b\right\} = \sum_{r=1}^{3} \int_{h_r - z_0}^{h_{r+1} - z_0} \left[\in_{11}^b, \in_{22}^b\right] \sin^2\left(\frac{\pi \bar{z}_{ns}}{h_p}\right) dz_{ns} \tag{53}$$

$$\left\{A_{33}^b, B_{33}^b, I_{33}^b\right\} = \sum_{r=1}^{3} \int_{h_r - z_0}^{h_{r+1} - z_0} \left[C_{33}^b g'^2(z_{ns}), \frac{\pi}{h_p} e_{33}^b g'(z_{ns}) \sin\left(\frac{\pi \bar{z}_{ns}}{h_p}\right), \frac{\pi^2}{h_p^2} \in_{33}^b \sin^2\left(\frac{\pi \bar{z}_{ns}}{h_p}\right)\right] dz_{ns} \tag{54}$$

$$\begin{Bmatrix} A_{ij}^s & B_{ij}^s & J_{ij}^s \\ F_{ij}^s & R_{ij}^s & L_{ij}^s \end{Bmatrix} = C_{ij}^s \begin{Bmatrix} 1 & z_{ns} & z_{ns}^2 \\ f(z_{ns}) & z_{ns}f(z_{ns}) & f^2(z_{ns}) \end{Bmatrix} \Bigg|_{z_{ns} = \pm\frac{h_c}{2} \pm h_p - z_0} \quad i,j = 1,2,6 \tag{55}$$

$$\left\{D_{ii}^s, E_{ii}^s\right\} = \left[C_{13}^s g'(z_{ns}), \frac{\pi}{h_p} e_{13}^s \sin\left(\frac{\pi \bar{z}_{ns}}{h_p}\right)\right] \left\{1, z_{ns}, f(z_{ns})\right\} \Bigg|_{z_{ns} = \pm\frac{h_c}{2} \pm h_p - z_0} \quad i = 1,2,3 \tag{56}$$

$$\left\{I_{11}^s, I_{22}^s\right\} = \left[\in_{11}^s, \in_{22}^s\right] \sin^2\left(\frac{\pi \bar{z}_{ns}}{h_p}\right) \Bigg|_{z_{ns} = \pm\frac{h_c}{2} \pm h_p - z_0} \tag{57}$$

$$\left\{A_{33}^s, B_{33}^s, I_{33}^s\right\} = \left[C_{33}^s g'^2(z_{ns}), \frac{\pi}{h_p} e_{33}^s g'(z_{ns}) \sin\left(\frac{\pi \bar{z}_{ns}}{h_p}\right), \frac{\pi^2}{h_p^2} \in_{33}^s \sin^2\left(\frac{\pi \bar{z}_{ns}}{h_p}\right)\right] \Bigg|_{z_{ns} = \pm\frac{h_c}{2} \pm h_p - z_0} \tag{58}$$

$$\left\{H_{11}^s\right\} = \left\{H_{22}^s\right\} = \left[e_{15}^s g(z_{ns}) \cos\left(\frac{\pi \bar{z}_{ns}}{h_p}\right)\right] \Bigg|_{z_{ns} = \pm\frac{h_c}{2} \pm h_p - z_0} \tag{59}$$

$$\left\{P_{11}^s\right\} = \left[\tau_s g(z_{ns})\right] \Big|_{z_{ns} = \pm\frac{h_c}{2} \pm h_p - z_0} \tag{60}$$

3   SOLUTION PROCEDURE OF SIMPLY-SUPPORTED NANO-PLATE

It is necessary to define the electrical field and five mechanical displacements, before detailing the solution procedure. Hence, according to Navier's solution procedure, an analytical method is used to solve the motion equations. To achieve this, six unknown functions can be assumed employing trigonometric functions in terms of the double-Fourier series as follows [14,63]:

$$u(x,y,t) = U_{mn}\cos(\alpha x)\sin(\beta y)$$
$$v(x,y,t) = V_{mn}\sin(\alpha x)\cos(\beta y)$$
$$w_b(x,y,t) = W_{bmn}\sin(\alpha x)\sin(\beta y)$$
$$w_s(x,y,t) = W_{smn}\sin(\alpha x)\sin(\beta y)$$
$$\varphi(x,y,t) = \Phi_{mn}\sin(\alpha x)\sin(\beta y)$$
$$\phi(x,y,t) = \Theta_{mn}\sin(\alpha x)\sin(\beta y)$$

(61)

In this Eq., the unknown coefficients are defined as $\{U_{mn}, V_{mn}, W_{bmn}, W_{smn}, \Phi_{mn}, \Theta_{mn}\}$. Also $\alpha = m\pi/a$ and $\beta = n\pi/b$ are constant coefficients related to the mode numbers (m,n) in x and y directions, respectively. Substituting the admissible displacement functions of Eq. (61) into the equation of motion, one obtains the analytical solution for buckling analysis of sandwich nano-plate with FG core and piezoelectric face-sheets in the following matrix form:

$$([K] - [S])\{X_{mn}\} = 0$$

(62)

It should be noted that the $\{X_{mn}\}$ describes unknown coefficients and also $[K]$ and $[S]$ represents the stiffness and in-plane forces matrixes. To determine the critical buckling load versus different changing parameters, it is necessary to analyze the behavior of the structure under different conditions. Hence, one must calculate the determinant of the coefficient matrix in Eq. (62) and set it to zero. Finally, the critical buckling load is identified as the smallest eigenvalue obtained from this calculation.

$$\det([K] - [S]) = 0$$

(63)

4   NUMERICAL RESULTS AND DISCUSSION

The numerical results highlight the bi-axial buckling behavior of an FG nano-plate integrated with piezoelectric face sheets, utilizing surface piezoelasticity theory. In the subsequent examples, the FG nano-plate is assumed to consist of aluminum and alumina [52,64]. Conversely, the piezoelectric face sheets are considered to be composed of materials whose bulk and surface properties [60]. The following analyses use common values for consistency.

$$E_m = 70\,GPa, E_c = 380\,GPa, \upsilon = 0.3$$
$$\mu = \ell = 1(nm), V_0 = -5(v), k = 1, a/b = 2, h = 3(nm), \tau_s = 1(N/m), m = n = 1,$$
$$K_w = 1^{\wedge}17(N/m^3), \theta = \pi/4, K_{gx} = 10(N/m), K_{gy} = 20(N/m), h_c/h_p = 10$$

Table 1
Comparison of the buckling load of FG plate for various power-law index

| k | Model | Axial/Bi-axial | Non-dimensional critical buckling load | | | | | |
			1-0-1	2-1-2	2-1-1	1-1-1	2-2-1	1-2-1
0	Ref. [52]	Axial	13.00552	13.00552	13.00552	13.00552	13.00552	13.00552
	Present Model		13.00552	13.00552	13.12398	13.00552	13.07977	13.00552
	Ref. [52]	Bi-axial	6.50276	6.50276	6.50276	6.50276	6.50276	6.50276
	Present Model		6.50326	6.50425	6.56199	6.50276	6.53988	6.50280
1	Ref. [52]	Axial	5.16629	5.83941	6.19371	6.46450	6.94952	7.50719
	Present Model		5.16712	5.84012	6.21936	6.46750	6.96728	7.50991
	Ref. [52]	Bi-axial	2.58315	2.91970	3.09686	3.23225	3.47476	3.75359
	Present Model		2.58317	2.92010	3.10968	3.23245	3.48364	3.75652
5	Ref. [52]	Axial	2.65679	3.04141	3.40280	3.57873	4.11157	4.73463
	Present Model		2.65600	3.04527	3.41752	3.57900	4.12120	4.73785
	Ref. [52]	Bi-axial	1.32839	1.52071	1.70140	1.78937	2.05578	2.36731
	Present Model		1.32840	1.52070	1.70876	1.79136	2.06060	2.37011
10	Ref. [52]	Axial	2.48574	2.74498	3.09111	3.19373	3.70686	4.27964
	Present Model		2.48998	2.74652	3.10632	3.19993	3.71037	4.28215
	Ref. [52]	Bi-axial	1.24287	1.37249	1.54556	1.59687	1.85343	2.13982
	Present Model		1.24381	1.37989	1.55316	1.60120	1.85915	2.14001

To ensure the validity and accuracy of the model used, a comprehensive comparison is essential. Consequently, the accuracy of the presented plate theory and appropriateness of the solution approach are assessed by simulating the response of the dimensionless buckling load of the sandwich plate with different thickness ratios as presented in Table 1 [50]. In addition, Fig. 3 presents a comparison study of bi-axial normalized buckling load of the FG simply supported square plate according to the ratio of the length to the thickness of structure. It can be seen that the critical buckling loads decrease as the material index increases. Conversely, the length-to-thickness ratio positively impacts the critical buckling loads, enhancing the structure's stability. It is evident from Table 1 and Fig. 3 that the numerical results have excellent agreements with the obtained results in available references [50]. On the other hand, a comparison of nondimensional critical buckling load for square plate under different the material index and length-to-thickness ratio is presented in Table 2. In this Table, the results based on the various theories with the present model have been examined according to length-to-thickness ratio and power low index. Table 2 shows that there is a good agreement between the existing results and the proposed model under various loading conditions.
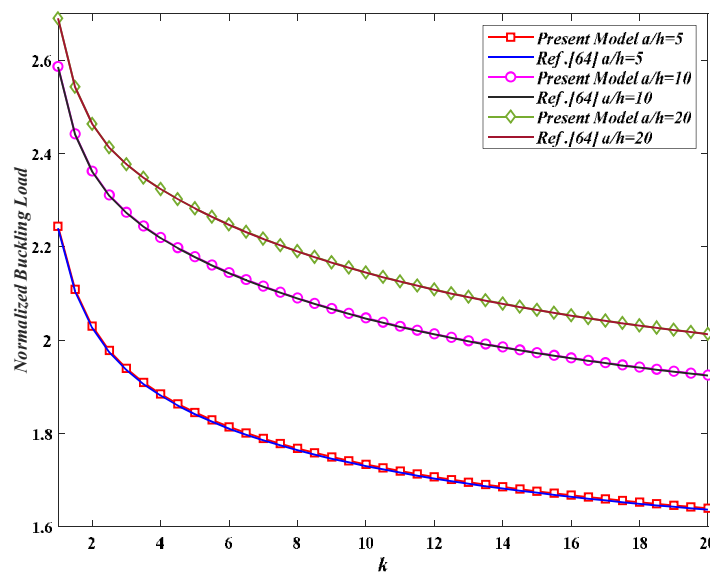

Fig. 3
Effects of material index on the critical buckling loads of simply supported square plate versus length-to-thickness ratio

Table 2
Comparison of the buckling load of FG plate for various power-law index

k	a/H	Model						
		Ref. [65]	Ref. [37]	Ref. [38]	Ref. [55]	Ref. [63]	Ref. [64]	Present Model
0.1	5	2.8905	2.8949	2.9028	2.9287	2.9003	2.8946	2.9910
	10	3.3470	3.3484	3.3513	3.3682	3.3502	3.3515	3.4591
	20	3.4983	3.4986	3.4991	3.5068	3.4990	3.5010	3.6002
	50	3.5502	3.5502	3.5502	3.5518	3.5503	3.5508	3.6419
0.5	5	2.4143	2.4180	2.4246	2.4459	2.4225	2.4176	2.5157
	10	2.7949	2.7961	2.7985	2.8123	2.7976	2.7985	2.8956
	20	2.9207	2.9209	2.9214	2.9276	2.9213	2.9229	3.0095
	50	2.9638	2.9638	2.9638	2.9651	2.9638	2.9643	3.0430
2	5	2.0003	2.0024	2.0077	2.0249	2.0059	2.0031	2.0300
	10	2.3518	2.3525	2.3546	2.3660	2.3538	2.3549	2.3621
	20	2.4694	2.4695	2.4699	2.4752	2.4698	2.4713	2.4631
	50	2.5097	2.5097	2.5097	2.5109	2.5097	2.5102	2.4930
10	5	1.6878	1.6910	1.6966	1.7125	1.3949	1.6898	1.7334
	10	1.9929	1.9940	1.9962	2.0064	1.9954	1.9954	2.0474
	20	2.0956	2.0958	2.0963	2.1011	2.0962	2.0972	2.1449
	50	2.1310	2.1310	2.1310	2.1321	2.1311	2.1314	2.1739

The size-dependent behavior of FG nano-plate based on thethickness-to-length ratio and thematerial characteristic parameter is shown in Fig. 4. As thethickness-to-length ratio increases, the critical buckling load generally increases for all values of length scale parameters. On the other hand, the curves for different values of length scale parameters appear to diverge, indicating that higher values of length scale parameters led to greater critical buckling loads. The length scale parameter is vital in estimating the critical load values of nanostructures. As discussed in the mathematical modeling section, this study applies the parameter using NSGT. Increasing the length scale parameter enhances the structure's stiffness and raises the critical load, thus improving the structure's static stability. The inclusion of thelength scale parameter leads to an increase in thecritical buckling load of theFG nano-plate, especially in the higher thickness-to-length ratios. Increasing the thickness-to-length ratio in structures generally enhances their stiffness and strength. This increase in thickness relative to length raises the structure's resistance to bending forces and compressive loads, which in turn reduces the likelihood of buckling in the system. As a result, structures can withstand higher loads without undergoing unstable deformations. Essentially, this change boosts the overall stability and resistance of the structure against sudden and variable loads.

The relationship between the critical buckling load and the ratio of thickness to length for different values of nonlocal parameters are shown in Fig. 5. The nonlocal parameters exhibit a stiffness-softening influence on FG nano-plate structures. Applying non-local theory reduces the critical buckling load of FG nano-plates. Increasing the nonlocal parameter decreases the stiffness of the sandwich nano-plate, thereby lowering its critical buckling load. This trend suggests that increasing the thickness-to-length ratio enhances the load-bearing capacity of the structure, which is crucial for design considerations in engineering applications. This graph indicates that the critical buckling load is positively correlated with the nonlocal parameter, meaning that as nonlocality increases, the structural resistance to buckling also increases. This type of analysis is important in fields such as structural engineering and materials science, where understanding the stability and load-bearing capacity of structures is crucial. As can be seen from Figs. 4 and 5, the influence of the nonlocal parameter and the length scale coefficient due to the consideration of the NSGT is more prominent in higher ratios of the thickness to the length of the nanostructure.
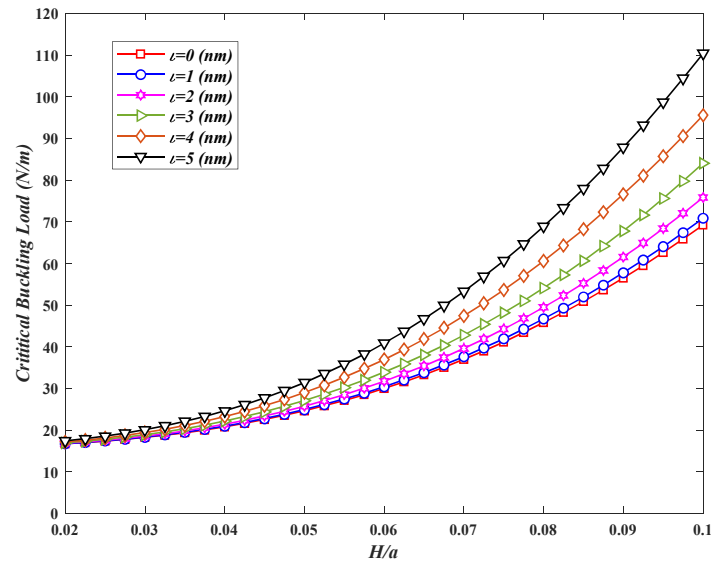
Fig. 4
Effects of thickness-to-length ratio on the buckling load for various length scale parameters.
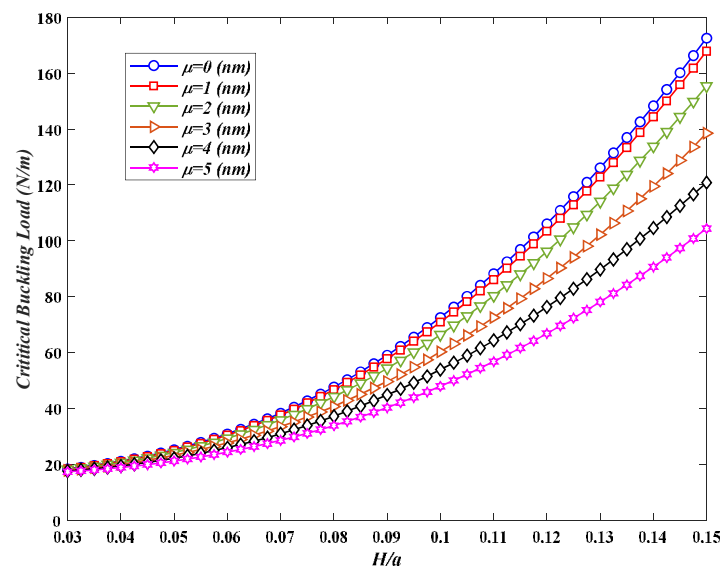
Fig. 5
Effects of the thickness-to-length ratio on the critical buckling load concerning different nonlocal parameters.

Fig. 6 shows the buckling results of FG nano-plate various length-to-width ratios and the core-to-face-sheets thickness, simultaneously. It is evident that maintaining a constant total thickness alongside the core's nonhomogeneous parameter results in a thicker core, which inevitably reduces the thickness of the piezoelectric layer. Since the stiffness of the core is significantly greater than that of the piezoelectric face sheets, an increase in core thickness enhances the overall structural stiffness, thereby elevating the critical load capacity. Conversely, an increase in the length-to-width ratio of the nano-plate exerts a profound influence on the reduction of the nano-plate's stiffness, which subsequently diminishes the buckling load. Generally, elongating the structure about its width alters its geometric configuration and ultimately modifies the behavior of the nano-sandwich plate. As the length-to-width ratio of the nano-plate increases, the structural response increasingly resembles that of a beam model, leading to a reduction in the variability of buckling behavior in this state. Increasing the length-to-width ratio of a structure significantly reduces its stiffness. This reduction in stiffness makes the structure less resistant to compressive loads, leading to a decrease in buckling load. Essentially, as the length increases relative to the width,

the overall shape of the structure changes, and its behavior tends to resemble that of a beam. In this state, the changes in buckling behavior also diminish. Greater length compared to width makes the structure generally more flexible and sensitive to compressive forces.
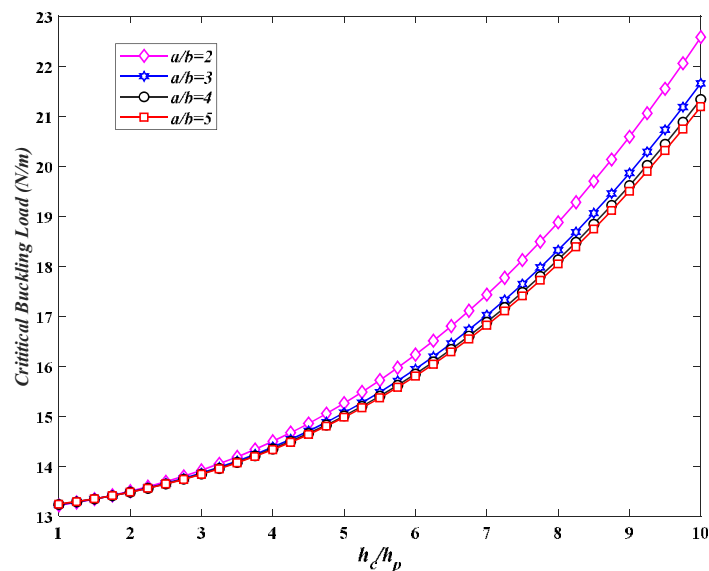
Fig. 6
Critical buckling load of FG sandwich nanoplate versus aspect ratio for various core-to-face-sheet thicknesses ratio.

Fig. 7 examines the influences of the thickness ratio on size-dependent critical buckling load of non-local sandwich nano-plate via versus gradient index parameter according to the refined plate theory. The essential load increases with the increasing value of the thicknesses of face sheets. According to this figure, an increase in the power-law index leads to an increase/decrease in metallic/ceramic properties along the thickness of the structure. Due to the lower elastic modulus and as a result the stiffness of the metal material compared to the ceramic material, the rigidity of the core is reduced and as a result, the critical load of the structure is reduced. According to the material considered for the FG core, decreasing the thickness of the core compared to the total thickness leads to an increase in the stiffness of the structure and an improvement in the critical load. The results indicate that increasing the power index has minimal impact on essential changes of load, despite the increase in the ratio of thicknesses.

The simultaneous investigation of the influences of the length-to-width ratio of the nanoplate as well as the core-to-total thickness ratio on the static stability behavior of the three-layer FG nanoplate considering different gradient index is presented in Table 3. As the value of the gradient index increases, the critical buckling load tends to increase for most configurations and parameter values. Different configurations (e.g., (1,1), (1,2), (2,2)) show varying responses to changes in the gradient index and the other parameters, indicating that the structural characteristics are sensitive to these variables. This table provides valuable insights into how different configurations and parameters affect the critical buckling load, which is essential for designing stable structures. Understanding these relationships can help in optimizing materials and geometries for better performance under load.
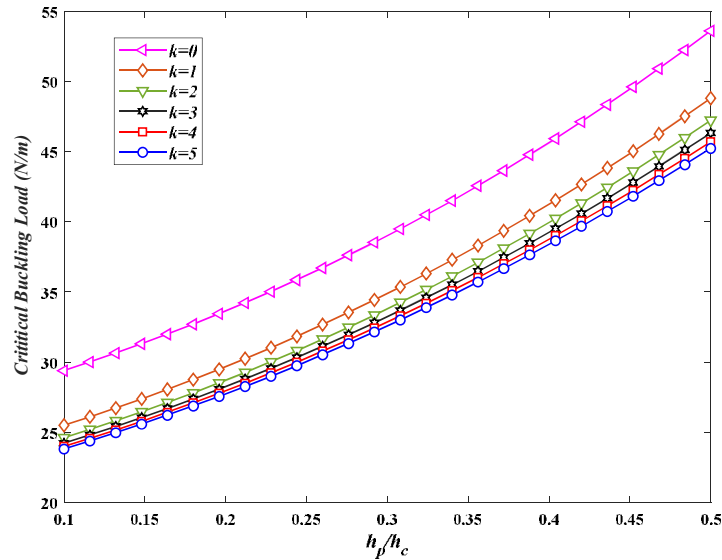
Fig. 7
Influence of the face sheet-to-core thickness ratio on critical buckling load of nanoplate with respect gradient index.

Table 3
Buckling critical load of FG nanoplate based on aspect ratio considering power index and different wave numbers nondimensional-dimensional

(m,n)	a/b	h_c/H	k			
			1	2	5	10
(1,1)	2	0.5	15.64350634	15.60132555	15.54776962	15.51090450
		0.6	17.25490354	17.12981230	16.97903363	16.87645336
		0.75	25.82962251	24.90650709	23.87214729	23.23813339
	5	0.5	15.49193132	15.45859392	15.41691875	15.38797133
		0.6	16.87143167	16.77151698	16.65318329	16.57176205
		0.75	24.22568562	23.47844273	22.65552815	22.14196354
	10	0.5	15.47779502	15.44563243	15.40550753	15.37760413
		0.6	16.82504462	16.72852869	16.61447763	16.53588029
		0.75	24.00634458	23.28334972	22.48888969	21.99178808
(1,2)	2	0.5	20.08414769	19.81139008	19.42623867	19.18583476
		0.6	25.01041060	24.30725170	23.34285931	22.76068580
		0.75	48.42747023	44.33706612	39.20202250	36.55772686
	5	0.5	19.83400568	19.57862913	19.21808933	18.99232956
		0.6	24.58392001	23.92337575	23.01741112	22.46804026
		0.75	47.23690701	43.35998972	38.48410476	35.95672702
	10	0.5	19.79878747	19.54583360	19.18872395	18.96501308
		0.6	24.52356958	23.86899872	22.97121827	22.42646336
		0.75	47.06631604	43.21973897	38.38065813	35.86998848
(2,2)	2	0.5	21.01428752	20.67387514	20.19304902	19.89652875
		0.6	26.57009320	25.70441803	24.51717843	23.81205051
		0.75	52.59241212	47.72970942	41.65767444	38.60047000
	5	0.5	19.97621015	19.71099092	19.33651401	19.10244957
		0.6	24.8268220	24.14209532	23.20298211	22.63496900
		0.75	47.9180978	43.91940982	38.89573475	36.30152732

	0.5	19.83400568	19.57862913	19.21808933	18.99232956
10	0.6	24.58392001	23.92337575	23.01741112	22.46804026
	0.75	47.23690701	43.35998972	38.48410476	35.95672702

Fig. 8 illustrates the size-dependent behavior of sandwich FG nanoplate with piezoelectric face sheets based on the surface elasticity theory and quasi-3D theory according to the ratio of the width to the length of the structure. As the results show, considering the effects of the surface increases the stiffness of the structure and thus increases the criticality of the structure. The results indicate that the decreasing trend is more pronounced at lower width-to-length ratios. This is because the presence of surface elasticity enhances flexural rigidity. In other words, considering surface piezoelectricity makes the nano-plate stiffer, which increases the critical load. The findings highlight that surface effects significantly impact the critical buckling load and should not be overlooked. This information is crucial for understanding the stability of structures under various loading conditions and geometric configurations.
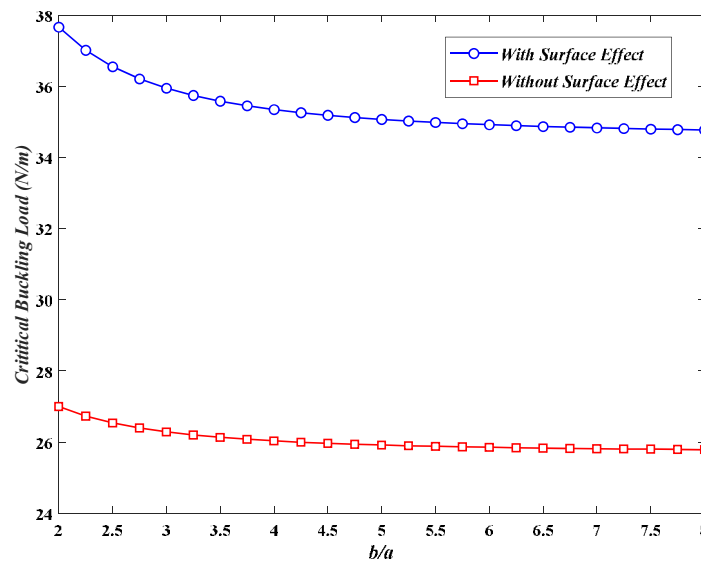

Fig. 8
Variation of critical buckling load FG sandwich piezoelectric nanoplate based on surface effect parameters.

The impact of the stretching effect alongside the effect of the thickness-to-length ratio on the critical buckling load of non-local FG nano-plates resting on an elastic foundation is illustrated in Fig. 9. It's evident from the figure that accounting for the stretching effect decreases the critical buckling load. It can be seen from the comparison of the two presented models that at low thickness-to-length ratios, both models predict similar outcomes. However, as this ratio increases, their predictions diverge significantly. This indicates that the quasi-3D model, which includes more detailed parameters, provides more realistic results compared to the simplified 2D model. This means that when the stretching effect is considered, the structure becomes less capable of withstanding buckling under pressure. The stretching effect is directly related to the thickness of the nano-plate. As the thickness increases, the influence of the stretching effect becomes more pronounced, affecting the overall stiffness and critical load. In essence, the adjustments made in the quasi-3D model incorporate more complex factors, leading to more accurate predictions of the structure's behavior under stress, particularly as the thickness-to-length ratio changes. This improved modeling accounts for the real-world influences of surface elasticity and stretching, providing a deeper understanding of how these factors affect the nano-plate's stability.

Fig. 10 depicts the relationship between the critical buckling load, boundary conditions, and the ratio of thickness to the width of the sandwich nanoplate. The CCCC condition exhibits the highest critical buckling load at any given thickness□to□width ratio value, followed by CSCS and then SSSS, indicating that the boundary conditions significantly influence the stability of the structure. Fully Supported condition shows the highest critical buckling load because all edges are fully supported, which increases resistance to buckling. CSCS and SSSS boundary conditions bear lower loads, as some edges are free, reducing stiffness and increasing the likelihood of buckling. As the ratio thickness□to□width ratio changes, the stress distribution in the member also varies. In cases with greater height, compressive stresses are distributed more uniformly, leading to higher critical loads. On the

other hand, the overall stiffness of a member depends on its dimensions and boundary conditions. An increase in the thickness☐to☐width ratio usually leads to increased stiffness and, consequently, higher critical loads. With higher critical loads, the likelihood of buckling decreases, indicating enhanced stability of the structure.
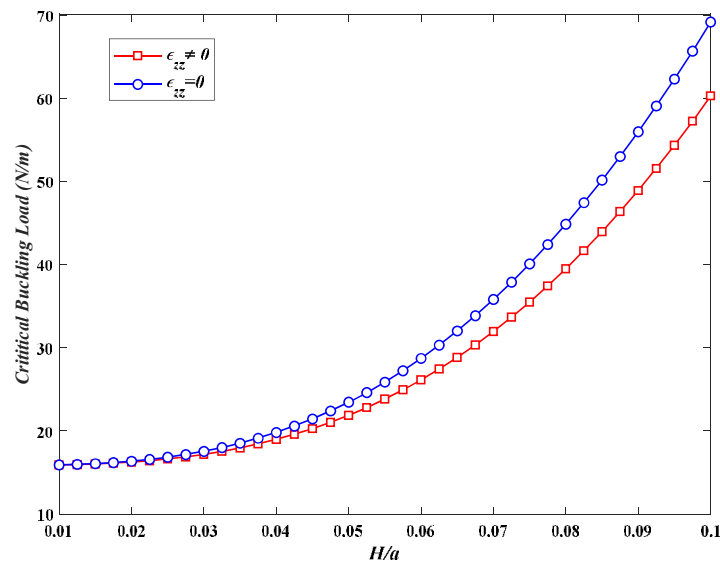
Fig. 9
Response of buckling load versus thickness-to-length ratio with and without stretching effect.

The behavior of critical load of non-local FG nano-plate with piezoelectric face-sheets based on quasi-3D theory according to the versus boundary conditions, face sheet-to-total thickness ratio, and applied initial voltage is presented in Table 4. The results show that the fully clamped boundary condition consistently shows the highest critical buckling loads across all configurations and loading conditions. The clamping provides maximum resistance to buckling, leading to higher loads before failure. As the face sheet-to-total thickness ratio increases from 0.1 to 0.25, the critical buckling loads generally increase across all boundary conditions. This trend indicates that the structural capacity before buckling occurs is enhanced at the higher face sheet-to-total thickness. The data indicates that as the initial voltage increases from -20 to 20, the critical buckling loads tend to increase. Applying an initial electric load to a structure can significantly affect its behavior, particularly in nanostructures. An initial electric load can enhance the stiffness of structures like piezoelectric nanoplates. This increased stiffness is due to the internal stresses generated by the electric load, which improves the structure's resistance to deformation. The initial electric load can significantly influence the stability of the structure. It may either enhance or diminish the stability against external loads. In some cases, a higher initial electric load can reduce the critical buckling load, thereby decreasing stability.
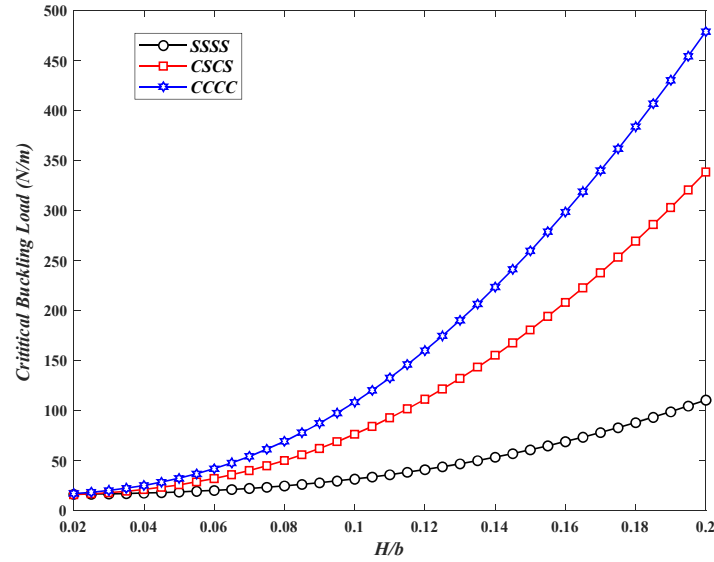
Fig. 10
The effect of boundary conditions and also thickness‐to‐width ratio on the buckling critical load of FG nanostructure

Table 4
The effect of boundary conditions, the thickness of face sheets, and the applied initial voltage on the critical buckling load

| B.C.	(m,n)	h_p/H	V_0				
			-20	-10	0	10	20
SSSS	(1,1)	0.1	65.90192	55.70192	45.50192	35.30192	25.10192
		0.15	78.79441	68.59441	58.39441	48.19441	37.99441
		0.25	132.95641	122.75641	112.55641	102.35641	92.15641
	(1,2)	0.1	117.17352	106.97352	96.77352	86.57352	76.37352
		0.15	143.06258	132.86258	122.66258	112.46258	102.26258
		0.25	221.48013	211.28013	201.08013	190.88013	180.68013
	(2,2)	0.1	125.27303	115.07303	104.87303	94.67303	84.47303
		0.15	152.04917	141.84917	131.64917	121.44917	111.24917
		0.25	228.11377	217.91377	207.71377	197.51377	187.31377
CSCS	(1,1)	0.1	101.54946	91.34946	81.14946	70.94946	60.74946
		0.15	123.89589	113.69589	103.49589	93.29589	83.09589
		0.25	200.28946	190.08946	179.88946	169.68946	159.48946
	(1,2)	0.1	162.06379	151.86379	141.66379	131.46379	121.26379
		0.15	189.95935	179.75935	169.55935	159.35935	149.15935
		0.25	249.14204	238.94204	228.74204	218.54204	208.34204
	(2,2)	0.1	164.35334	154.15334	143.95334	133.75334	123.55334
		0.15	191.22004	181.02004	170.82004	160.62004	150.42004
		0.25	255.72407	245.52407	235.32407	225.12407	214.92407
CCCC	(1,1)	0.1	116.06930	105.86930	95.66930	85.46930	75.26930
		0.15	141.02614	130.82614	120.62614	110.42614	100.22614
		0.25	219.95131	209.75131	199.55131	189.35131	179.15131
	(1,2)	0.1	170.98038	160.78038	150.58038	140.38038	130.18038
		0.15	198.54340	188.34340	178.14340	167.94340	157.74340
		0.25	255.40453	245.20453	235.00453	224.80453	214.60453
	(2,2)	0.1	172.09450	161.89450	151.69450	141.49450	131.29450

| 0.15 | 198.60430 | 188.40430 | 178.20430 | 168.00430 | 157.80430 |
| 0.25 | 261.67325 | 251.47325 | 241.27325 | 231.07325 | 220.87325 |

Fig. 11 illustrates the influence of surface effect on the size-dependent behavior of nano-sized plates based on refined plate theory. This Fig. indicates that surface effects play a significant role in improving the structural stability against buckling. As the ratio of thickness to the length increases, the impact of these surface effects becomes more pronounced, leading to higher critical loads. The presence of surface elasticity often leads to higher flexural rigidity in nano-sized sandwich structures. This means the structure becomes stiffer, which can increase its resistance to buckling. At the nanoscale, the surface area to volume ratio is much higher compared to macroscale structures. This results in surface effects becoming more pronounced. These effects can alter the mechanical properties of the materials involved, such as increasing the effective modulus of elasticity, which impacts the critical buckling load. The surface effects generally enhance the stiffness of the nano-sandwich structures, which in turn increases their stability. This means that the structures can sustain higher loads before buckling occurs. In general, surface effects are crucial in determining the buckling behavior of nano-sized sandwich structures, significantly impacting their stiffness, stability, and overall mechanical performance. Understanding and accurately modeling these effects are essential for the design and analysis of reliable nanoscale structures.
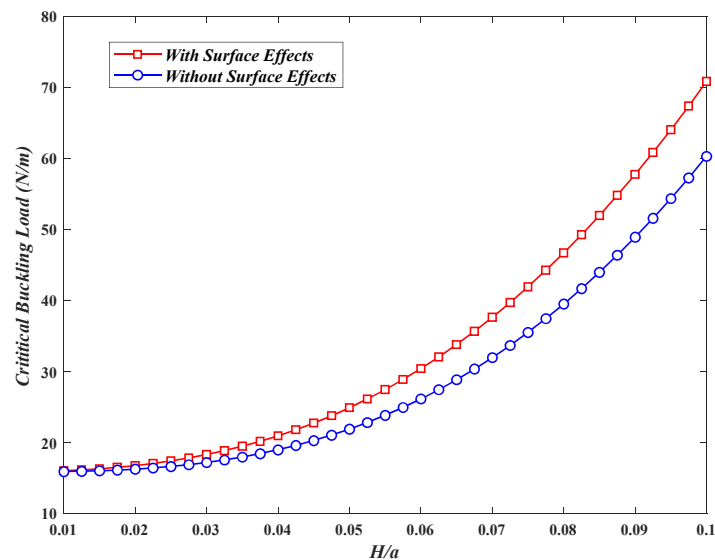
Fig. 11
Critical buckling load of the sandwich structure considering surface effects for various thickness☐to☐length ratios.

The non-local buckling behavior of the three-layer sandwich structure with FG core and piezoelectric layers based on the ratio of core thickness to length is presented in Fig. 12 to investigate the influence of the position of the neutral plane. The graph indicates that considering the neutral plane enhances the structural stability against buckling. As the core thickness-to-length ratio increases, the impact of this condition becomes more pronounced, leading to higher critical loads. This is because the core contributes to the load-bearing capacity and distributes stress more effectively across the structure. Overall, a thicker core improves the stability of FGMs. It helps in maintaining structural integrity under various load conditions, thus increasing the safety and reliability of the material in practical applications. The neutral plane acts as the axis where the compressive and tensile stresses are balanced. By balancing the internal stresses, the neutral plane increases the stability of the structure, making it more resistant to buckling and other forms of structural failure.
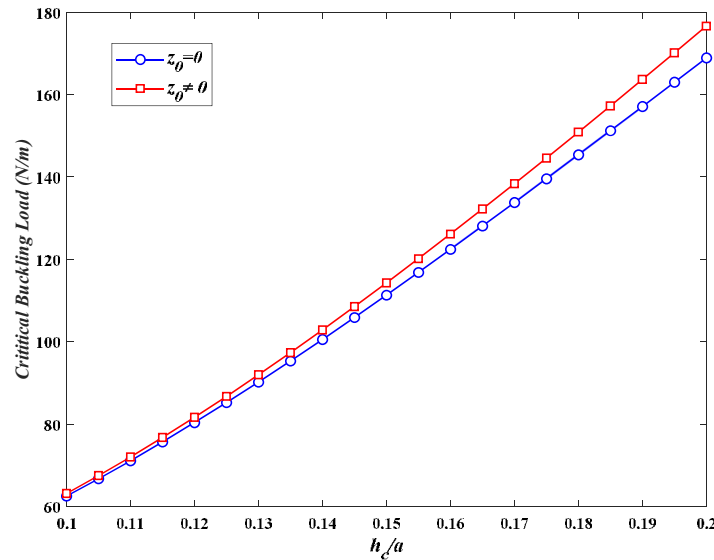
Fig. 12
The influence of neutral plate location and core thickness on buckling of sandwich nanoplate.
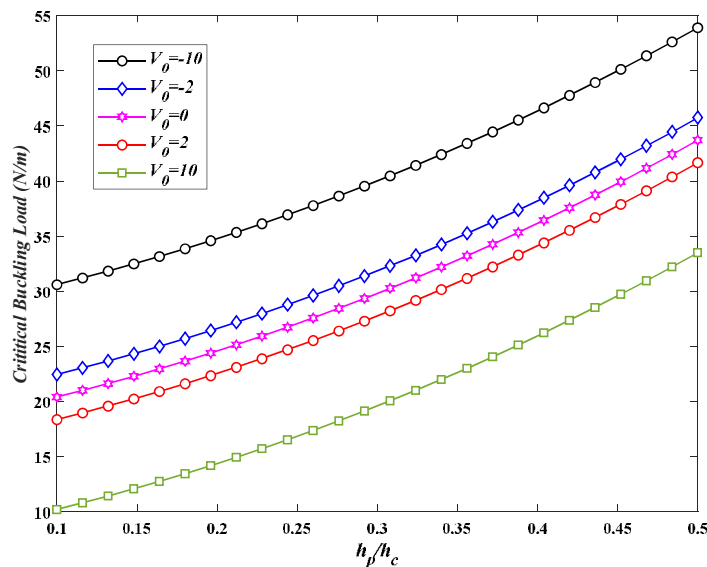
Fig. 13
Variation of buckling response concerning various thickness ratios and applied primary voltage.

The variations of buckling response sandwich nanoplate via piezoelectric face sheets subjected to an electric potential are investigated in Fig. 13 versus the electrical preload and thickness ratio. This Fig. shows that increasing the ratio of the thickness of the piezoelectric layers to the thickness of the FG core in a sandwich structure affects its buckling behavior significantly. A thicker piezoelectric face sheet compared to the FG core enhances the overall stiffness of the structure. This is because the face sheets, being more rigid, bear a larger portion of the load, thus increasing the structure's resistance to deformation. Based on Fig., electrical preloads can be categorized as tensile and compressive forces. The introduction of these preloads, influenced by external voltage, generates prestresses within the structure. When a negative voltage is applied, the stiffness of the structure increases, enhancing its static stability. Conversely, with a positive initial voltage, the stiffness diminishes, leading to a reduction in the structure's critical load.

The influence of the gradient index and the position of the neutral plane in the sandwich structure with a FG core is presented in Figure 14. In FGMs, the neutral surface shifts due to this non-uniform distribution, which can affect the mechanical performance of the material. The position of the neutral axis influences the overall strength and

stability of the material. If the neutral axis shifts toward a layer with a lower elastic modulus, it may lead to a decrease in strength and an increased risk of failure. In the design of structures such as composites, ceramics, and metals, understanding the impact of the neutral axis can help optimize performance and increase their lifespan. Additionally, Fig. 14 illustrates an increase in the power-law index, which affects the metallic and ceramic properties across the thickness of the structure. The lower elastic modulus of the metal compared to the ceramic results in reduced stiffness in the core, consequently lowering the critical load that the structure can withstand.
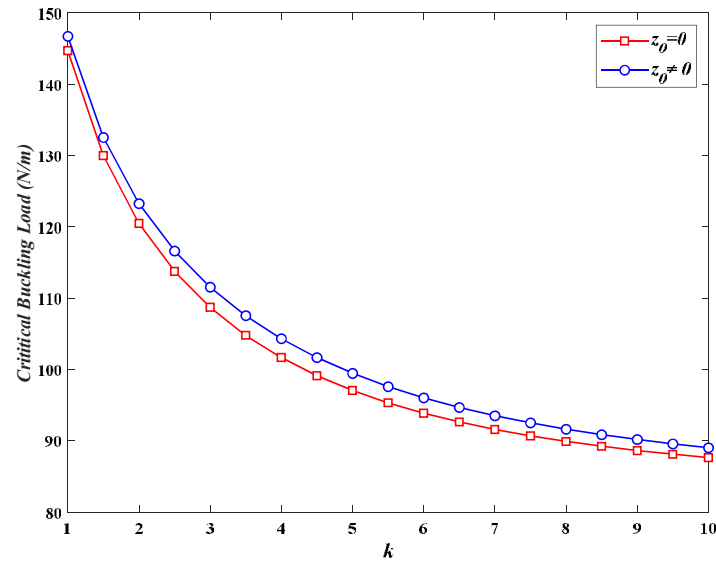
Fig. 14
Effects of gradient index and position of the neutral surface on the buckling load of nanoplate.

The effect of simultaneous initial voltage and gradient index on the buckling of a three-layer nanostructure consisting of a FG core and piezoelectric face sheets under an electric field is shown in Figure 15. The combined effects of initial voltage and gradient index can significantly influence the behavior of a structure, particularly in nanoscale and smart materials like FG and piezoelectric materials. Applying an initial voltage creates an electric field within the piezoelectric material. This field interacts with the mechanical properties, affecting the overall stiffness and stability of the structure. The presence of an initial voltage can either increase or decrease the critical buckling load, depending on the polarity and magnitude of the voltage. A higher gradient index typically means more significant variations in material properties, leading to more pronounced changes in stiffness and deformation behavior under the applied voltage.

Table 5 shows the numerical results of the buckling of the FG nanoplate by considering the surface effects according to the parameters related to the NSGT. In this table, the simultaneous effect of length scale parameters, non-local parameters, location of the neutral surface for the FG core, and surface effects are investigated. The combination of these factors creates a complex interplay that influences the overall mechanical behavior of the structure. Each parameter contributes to the stability, stiffness, and critical load capacity in different ways.
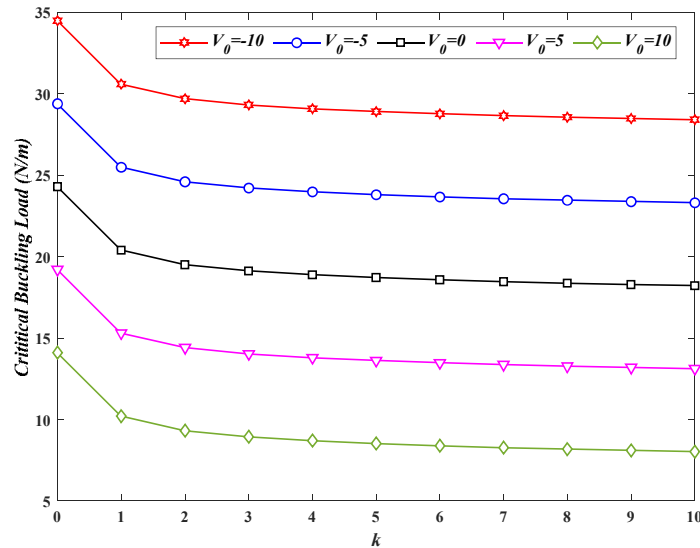
Fig. 15
The variations of buckling response versus power low index and primary applied voltage.

Table 5
Comparison of the critical buckling load of the nanoplate versus surface and NSGT effects

$\iota(nm)$	Surface Effect	z_0	$\mu(nm)$			
			1	2	3	4
1	With Surface Effect	$z_0 \neq 0$	35.1041499	29.7281064	24.9584852	21.6051111
		$z_0 = 0$	35.0418850	29.6812718	24.9253403	21.5815912
	Without Surface Effect	$z_0 \neq 0$	27.6381538	24.1123129	20.9841899	18.7849028
		$z_0 = 0$	27.5938679	24.0790018	20.9606156	18.7681742
2	With Surface Effect	$z_0 \neq 0$	42.2527191	35.1051368	28.7638079	24.3054145
		$z_0 = 0$	42.1686281	35.0418850	28.7190446	24.2736499
	Without Surface Effect	$z_0 \neq 0$	32.3256329	27.6381538	23.4794264	20.5555530
		$z_0 = 0$	32.2667563	27.5938679	23.4480852	20.5333129
3	With Surface Effect	$z_0 \neq 0$	54.1670011	44.0668542	35.1060124	28.8059201
		$z_0 = 0$	54.0465332	43.9762403	35.0418850	28.7604145
	Without Surface Effect	$z_0 \neq 0$	40.1380979	33.5145553	27.6381538	23.5066367
		$z_0 = 0$	40.0549037	33.451978	27.5938679	23.4752108
4	With Surface Effect	$z_0 \neq 0$	70.8469959	56.6132585	43.9850987	35.1066280
		$z_0 = 0$	70.6756005	56.4843378	43.8938616	35.0418850
	Without Surface Effect	$z_0 \neq 0$	51.0755491	41.7415173	33.4603722	27.6381538
		$z_0 = 0$	50.9583100	41.6533321	33.3979636	27.5938679

Fig. 16 depicts the critical buckling load of a square FG nano-plate for various elastic foundations according to the nonlocal refined plate theory. The results presented in this Fig. are extracted in the case that the surface area of the sandwich nanoplate is assumed to be constant. The ratio of the length to the width of the structure is considered a fixed value. As the results show, the lowest critical buckling load corresponds to the case where the structure is considered square. An elastic foundation provides additional support to the sandwich structure, which enhances its overall stability. The elastic foundation acts as a cushion that absorbs and redistributes applied loads, leading to better stress distribution within the structure. This can help mitigate the concentration of stresses in particular areas, which are common precursors to buckling. The figure illustrates that the buckling load of the rectangular nano-plate increases when an elastic medium is considered. It indicates that the highest critical buckling load is associated with

the orthotropic medium. This is because the Orthotropic Pasternak model effectively accounts for both transverse shear and normal loads of the elastic medium, while also accommodating an arbitrarily oriented foundation. It is evident that choosing the appropriate elastic medium is crucial for system stability, as it enhances the stiffness and overall stability of the system.

The influence of the shear layer coefficient of the Pasternak foundation on the buckling behavior of nanoplate based on refined NSGT is shown in Fig. 17. The results illustrate that this parameter significantly affects the buckling behavior and overall stability of structures. The shear layer in the Pasternak foundation provides additional shear resistance to the structure, which helps in distributing shear stresses more effectively. With higher shear layer coefficients, the structure can support higher critical buckling loads. The shear layer also contributes to damping out vibrations, which can further stabilize the structure under dynamic loading conditions.
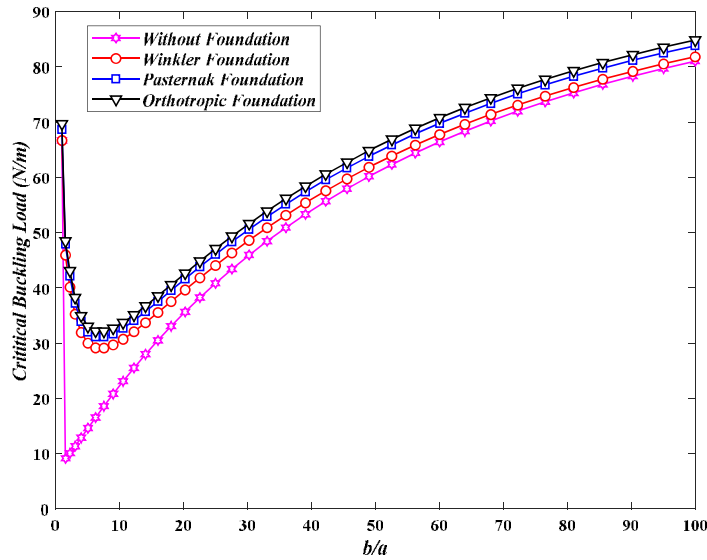
Fig. 16
The effect of different foundations on the critical buckling load of FG sandwich nanoplate
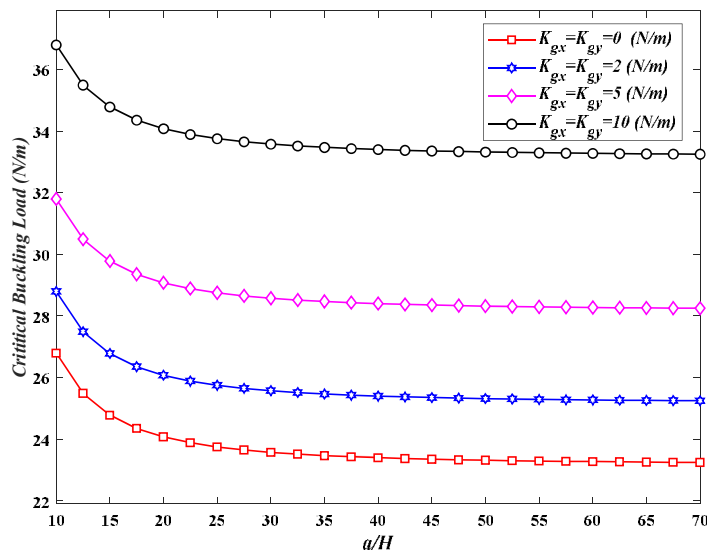
Fig. 17
The effect of various foundation shear layers on critical buckling load of nonlocal sandwich nano-plate

The influences of the orientation of the shear layer and orthotropic angle of foundation on the buckling responses of non-local plate integrated with two piezoelectric layers considering surface effect and NSGT are presented in

Figs. 18 and 19. The shear layer in the foundation provides additional resistance to shear forces, improving the structural stiffness. Orthotropic materials have different stiffness in different directions. Changing the orthotropic angle affects the stiffness and strength of the structure in specific directions. By tailoring the orthotropic angle, the load-bearing capacity can be maximized in desired directions, enhancing the overall performance of the structure. Accordingly, the selection of appropriate elastic medium parameters plays a crucial role in enhancing the stability and performance of the nano-plate.

Investigating the buckling behavior of sandwich structure with FG core and piezoelectric face sheets considering the NSGT based on different parameters of the foundation are comprehensively studied in Table 6. The elastic medium parameters significantly affect the critical buckling load. As these parameters increase, the critical buckling load also rises. This is because the elastic medium can act as a supporting factor, increasing resistance to deformation and failure.
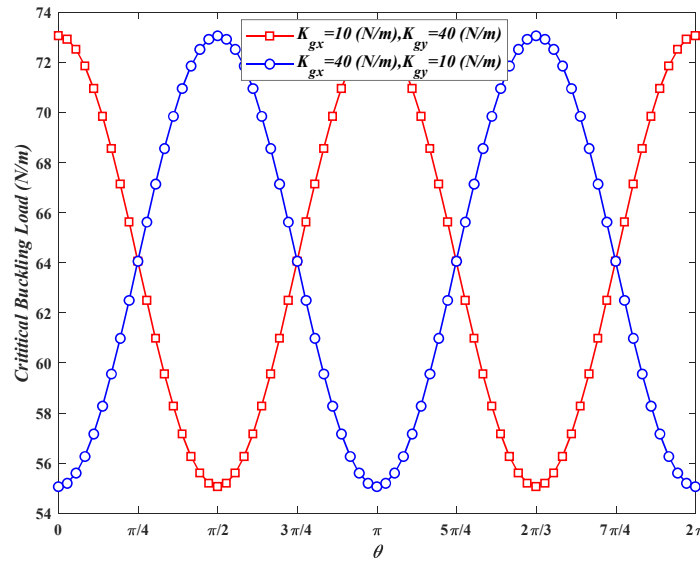

Fig. 18
The effect of orthotropic angle and shear coefficient of foundation on the buckling behavior of the structure
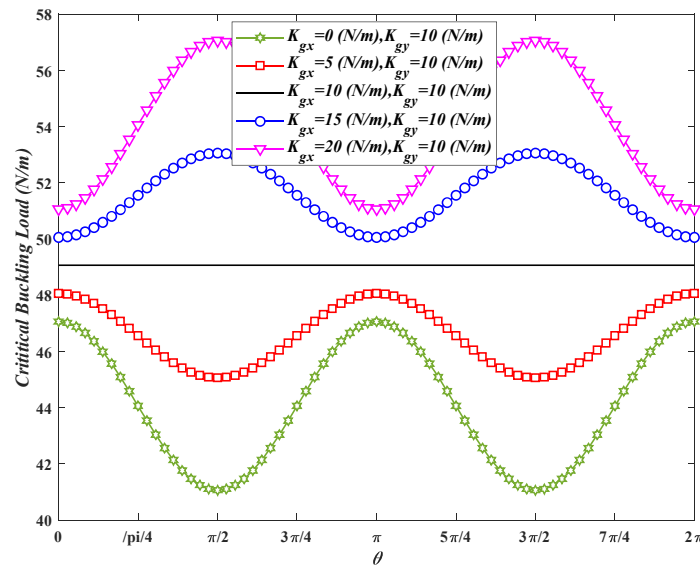

Fig. 19
The critical buckling load of the three-layer structure based on the orthotropic foundation according to the orthotropic angle and different parameters of the shear layer

Table 6
Numerical investigation of buckling load based on different parameters of the orthotropic Pasternak foundation.

$K_w (N/m^3)$	$K_{gx} (N/m)$	$K_{gy} (N/m)$	θ				
			0	$\pi/6$	$\pi/4$	$\pi/3$	$\pi/2$
		5	32.60	32.60	32.60	32.60	32.60
	5	10	36.60	35.85	35.10	34.35	33.60
		20	44.60	42.35	40.10	37.85	35.60
		5	33.60	34.35	35.10	35.85	36.60
$10*10^{16}$	10	10	37.60	37.60	37.60	37.60	37.60
		20	45.60	44.10	42.60	41.10	39.60
		5	35.60	37.85	40.10	42.35	44.60
	20	10	39.60	41.10	42.60	44.10	45.60
		20	47.60	47.60	47.60	47.60	47.60
		5	33.41	32.60	33.41	33.41	33.41
	5	10	37.41	35.85	35.91	35.16	34.41
		20	45.41	42.35	40.91	38.66	36.41
		5	34.41	34.35	35.91	36.66	37.41
$20*10^{16}$	10	10	38.41	37.60	38.41	38.41	38.41
		20	46.41	44.10	43.41	41.91	40.41
		5	36.41	37.85	40.91	43.16	45.41
	20	10	40.41	41.10	43.41	44.91	46.41
		20	48.41	47.60	48.41	48.41	48.41
		5	34.23	34.23	34.23	34.23	34.23
	5	10	38.23	37.48	36.73	35.98	35.23
		20	46.23	43.98	41.73	39.48	37.23
		5	35.23	35.98	36.73	37.48	38.23
$30*10^{16}$	10	10	39.23	39.23	39.23	39.23	39.23
		20	47.23	45.73	44.23	42.73	41.23
		5	37.23	39.48	41.73	43.98	46.23
	20	10	41.23	42.73	44.23	45.73	47.23
		20	49.23	49.23	49.23	49.23	49.23

5 CONCLUSIONS

In this study, an analytical solution based on a refined plate theory is developed to investigate the size-dependent buckling behavior of FG nano-plates integrated with piezoelectric face sheets resting on the orthotropic elastic medium by considering neutral surface position and surface effects. Eventually, the governing equations of the structure are derived by applying the theory of non-local strain gradient and considering the stretching effect by employing Hamilton's principle. The accuracy and efficiency of the present approach are validated through a review of comparison studies. The influences of several parameters such as thickness ratio, aspect ratio, power low index, orthotropic foundation, length scale and nonlocal parameters, surface effect, the position of the neutral surface, initial applied voltage, and various boundary conditions are examined on buckling responses of the three-layered nanoplate. The results revealed that increasing the thickness-to-length ratio generally enhances the critical buckling load due to improved structural stiffness and strength.

Additionally, the shear layer coefficient plays a significant role in enhancing shear resistance and distributing stresses, which supports higher critical buckling loads and contributes to vibration damping under dynamic conditions. The study also highlights the importance of boundary conditions, where fully clamped configurations yield the highest resistance to buckling. The relationship between the face sheet-to-total thickness ratio and

structural capacity further underscores the significance of these parameters in ensuring stability. The role of surface effects becomes more pronounced with increasing thickness-to-length ratios, leading to higher critical loads. The position of the neutral plane is also crucial for balancing internal stresses and enhancing stability against buckling. Overall, this research provides valuable insights for optimizing the design and analysis of nanostructured materials, emphasizing the need to consider various parameters to achieve superior structural performance and resilience under diverse loading conditions. Understanding these relationships is essential for advancing the development of stable and reliable nano-scale structures in engineering applications.

REFERENCES

[1]   Feri M., Krommer M., Alibeigloo A., 2021, Three-dimensional static analysis of a viscoelastic rectangular functionally graded material plate embedded between piezoelectric sensor and actuator layers, *Mechanics Based Design of Structures and Machines* **51(**7): 3843-3867.

[2]   Marzavan S., Nastasescu V., 2023, Free vibration analysis of a functionally graded plate by finite element method, *Ain Shams Engineering Journal* **14**(8): 102024.

[3]   Frahlia H., Bennai R., Nebab M., Ait Atmane H., Tounsi A., 2022, Assessing effects of parameters of viscoelastic foundation on the dynamic response of functionally graded plates using a novel HSDT theory, *Mechanics of Advanced Materials and Structures* **30**(13): 2765-2779.

[4]   Zargar Ershadi M., Faraji Oskouie M., Ansari R., 2022, Nonlinear vibration analysis of functionally graded porous circular plates under hygro-thermal loading, *Mechanics Based Design of Structures and Machines* **52**(2): 1042-1059.

[5]   Xie K., Chen H., Wang Y., Li L., Jin F., 2024, Nonlinear dynamic analysis of a geometrically imperfect sandwich beam with functionally graded material facets and auxetic honeycomb core in thermal environment, *Aerospace Science and Technology* **144**: 108794.

[6]   Arefi M., Soltan Arani A.H., 2018, Higher order shear deformation bending results of a magnetoelectrothermoelastic functionally graded nanobeam in thermal, mechanical, electrical, and magnetic environments, *Mechanics Based Design of Structures and Machines* **46**(6): 669-692.

[7]   Ghorbanpour Arani A., Kolahdouzan F., Abdollahian M., 2018, Nonlocal buckling of embedded magnetoelectroelastic sandwich nanoplate using refined zigzag theory, *Applied Mathematics and Mechanics* **39**(4): 529-546

[8]   Singh A.K., Koley S, Negi A., 2022. Remarks on the scattering phenomena of love-type wave propagation in a layered porous piezoelectric structure containing surface irregularity, *Mechanics of Advanced Materials and Structures* **30**(12): 2398-2429.

[9]   Dhua S., Mondal S., Maji A., 2024, Surface effects on wave propagation in piezoelectric–piezomagnetic loosely bonded bilayer system using nonlocal theory of elasticity, *thin wall structure* **197**: 111612.

[10]   Biswas M., Sahu S.A., 2022, Surface wave dispersion in imperfectly bonded flexoelectric-piezoelectric/FGPM bi-composite in contact of Newtonian liquid, *Mechanics of Advanced Materials and Structures* **30**(14): 2995-3012.

[11]   Mirzaei M., 2022, Vibration characteristics of sandwich plates with GPLRC core and piezoelectric face sheets with various electrical and mechanical boundary conditions, *Mechanics Based Design of Structures and Machines* **52**(2): 990-1013.

[12]   Hai T., Al-Masoudy M.M., Alsulamy S., El Ouni M.H., Ayvazyan A., Kumar A., 2023, Size-dependent free vibration analysis of honeycomb sandwich microplates integrated with piezoelectric actuators based on the modified strain gradient theory, *Composite Structures* **305**: p.116555.

[13]   Ghorbanpour Arani A., Jamali M., Mosayyebi M., Kolahchi R., 2016, Wave propagation in FG-CNT-reinforced piezoelectric composite micro plates using viscoelastic quasi-3D sinusoidal shear deformation theory, *Composites Part B: Engineering* **95**: 209-224.

[14]   Cao T.N.T., Reddy J.N., Lieu Q.X., Nguyen X.V., Luong V.H., 2021, A multi-layer moving plate method for dynamic analysis of viscoelastically connected double-plate systems subjected to moving loads, *advanced structural engineering* **24**(9): 1798-1813.

[15]   Ragb O., Matbulyb M.S., 2021, Nonlinear vibration analysis of elastically supported multi-layer composite plates using efficient quadrature techniques, *International Journal for Computational Methods in Engineering Science and Mechanics* **23**(2): 129-146.

[16]   Taghizadeh S.A., Naghdinasab M., Madadi H., Farrokhabadi A., 2021, Investigation of novel multi-layer sandwich panels under quasi-static indentation loading using experimental and numerical analyses, *Thin wall structure* **160**: 107326.

[17]   Amoozgar M., Fazelzadeh S.A., Ghavanloo E., Ajaj R.M., 2022, Free vibration analysis of curved lattice sandwich beams, *Mechanics of Advanced Materials and Structures* **31**(2): 343-355

[18]   Sahoo B., Sharma N., Sahoo B., Ramteke P.M., Panda S.K., Mahmoud S.R., 2022, Nonlinear vibration analysis of FGM sandwich structure under thermal loadings, *Structures* **44**: 1392-1402.

[19]   Derikvand M., Farhatnia F., Hodges H., 2021, Functionally graded thick sandwich beams with porous core: buckling analysis via differential transform method, *Mechanics Based Design of Structures and Machines* **51**(7): 3650-3677.

[20]   Li F., Yuan W., Zhang C., 2021, Free vibration and sound insulation of functionally graded honeycomb sandwich plates, *Journal of Sandwich Structures and Materials* **24**(1): 565-600.

[21]   Ghorbanpour Arani A., Shahraki M.E., Haghparast E., 2022, Instability analysis of axially moving sandwich plates with a magnetorheological elastomer core and GNP-reinforced face sheets, *journal of brazilian society of mechanical sciences and engineering* **44**(4):150

[22]   Li J., Kardomateas G., Liu L., 2023, Vibration analysis of thick-section sandwich structures in thermal environments, *international journal of mechanical sciences* **241**: 107937.

[23]   Liu S., Wang K., Wang B., 2023, Buckling and vibration characteristic of anisotropic sandwich plates with negative Poisson's ratio based on isogeometric analysis, *Mechanics Based Design of Structures and Machines* **9**:1-16.

[24]   Ren H., Zhuang X., Oterkus E., Zhu H., Rabczuk T., 2021, Nonlocal strong forms of thin plate, gradient elasticity, magneto-electro-elasticity and phase-field fracture by nonlocal operator method, *Engineering Computations* **39**: 23–44.

[25]   Pham Q.H., Nguyen P.C., Tran T.T., 2022, Dynamic response of porous functionally graded sandwich nanoplates using nonlocal higher-order isogeometric analysis, *Composite Structure* **290**: 115565,

[26]   Nguyen N.V., Phan D.H., 2023, A refined quasi-3D isogeometric model for dynamic instability of graphene nanoplatelets-reinforced porous sandwich plates, *aerospace science and technology* **142**: 108595.

[27]   Hung P.T., Phung-Van P., Thai C.H., 2023, Small scale thermal analysis of piezoelectric–piezomagnetic FG microplates using modified strain gradient theory, *International Journal of Mechanics and Materials in Design* **19**(4): 739-761.

[28]   Jin Q., 2021, Interlaminar stress analysis of functionally graded graphene reinforced composite laminated plates based on a refined plate theory, *Mechanics of Advanced Materials and Structures* **29**(25): 4138-4150.

[29]   Tharwan M.Y., Daikh A.A., Assie A.E., Alnujaie A., Eltaher M.A., 2023, Refined quasi-3D shear deformation theory for buckling analysis of functionally graded curved nanobeam rested on Winkler/Pasternak/Kerr foundation, *Mechanics Based Design of Structures and Machines* 1-24.

[30]   Hai Van N.T., Hong N.T., 2023, Novel finite element modeling for free vibration and buckling analysis of non-uniform thickness 2D-FG sandwich porous plates using refined Quasi 3D theory, *Mechanics Based Design of Structures and Machines* 1-27.

[31]   Shahmohammadi M.A., Azhari M., Salehipour H., Thai H.T., 2023, Buckling of multilayered CNT/GPL/fibre/polymer hybrid composite plates resting on elastic support using modified nonlocal first-order plate theory, *Mechanics Based Design of Structures and Machines* **52**(3): 1785-1810.

[32]   Ghandourah E.E., Daikh A.A., Alhawsawi A.M, Fallatah O.A., EltaherM.A., 2022, Bending and buckling of FG-GRNC laminated plates via quasi-3D nonlocal strain gradient theory, *Mathematics* **10**(8): 1321

[33]   Hung D.X., Van Long N., Tu T.M., Trung D.X., 2024, Bending analysis of FGSP nanoplate resting on elastic foundation by using nonlocal quasi-3D theory, *Thin Wall Structure* **196**: 111510.

[34]   Daikh A.A., Belarbi M.O., Khechai A., Li L., Ahmed H.M., Eltaher M.A., 2023, Buckling of bi-coated functionally graded porous nanoplates via a nonlocal strain gradient quasi-3D theory, *Acta Mechanica* **234**(8): 3397-3420.

[35]   Shahzad M.A., Sahmani S., Safaei B., Basingab M.S., Hameed A.Z., 2023, Nonlocal strain gradient-based meshless collocation model for nonlinear dynamics of time-dependent actuated beam-type energy harvesters at nanoscale, *Mechanics Based Design of Structures and Machine*s 1-35.

[36]   Mahmoudi A., Benyoucef S., Tounsi A., Benachour A., Adda Bedia E.A., Mahmoud, S.R., 2019, A refined quasi-3D shear deformation theory for thermo-mechanical behavior of functionally graded sandwich plates on elastic foundations, *Journal of Sandwich Structures and Materials* **21**(6): 1906-1929.

[37]   Karama M., Afaq K.S., Mistou S., 2009. A new theory for laminated composite plates. *Proceedings of the Institution of Mechanical Engineers. Part L, Journal of materials: Design and applications* **223**(L2): 53–62.

[38]   Nguyen-Xuan H., Thai C.H, Nguyen-Thoi T., 2013. Isogeometric finite Element analysis of composite sandwich plates using a higher order shear deformation theory. *Composites Part B Engineering* **55**: 558–74.

[39]   Meziane M.A.A., Abdelaziz H.H., Tounsi A., 2014, An efficient and simple refined theory for buckling and free vibration of exponentially graded sandwich plates under various boundary conditions, *Journal of Sandwich Structures and Materials* **16**(3): 293-318.

[40]   Bellifa H., Benrahou K.H., Hadji L., Houari M.S.A., Tounsi A., 2016, Bending and free vibration analysis of functionally graded plates using a simple shear deformation theory and the concept the neutral surface position, *Journal of the Brazilian Society of Mechanical Sciences and Engineering* **38**(1): 265-275.

[41]   Soltan Arani A.H., Ghorbanpour Arani A. and Khoddami Maraghi Z., 2024. Nonlocal quasi-3d vibration/analysis of three-layer nanoplate surrounded by Orthotropic Visco-Pasternak foundation by considering surface effects and neutral surface concept. *Mechanics Based Design of Structures and Machines* **52**(11): 9526-9561.

[42]   Barati M.R., Shahverdi H., 2017, An analytical solution for thermal vibration of compositionally graded nanoplates with arbitrary boundary conditions based on physical neutral surface position, *Mechanics of Advanced Materials and Structures* **24**(10): 840-853.

[43]   Farzam-Rad S.A., Hassani B., Karamodin A., 2017, Isogeometric analysis of functionally graded plates using a new quasi-3D shear deformation theory based on physical neutral surface, *Composites Part B: Engineering* **108**: 174-189.

[44]   Barati A., Norouzi S., 2020, Nonlocal elasticity theory for static torsion of the bi-directional functionally graded microtube under magnetic field, *Journal of Applied and Computational Mechanics* **51**(1): 30-36.

[45] Soleimani A., Zamani F., Haghshenas Gorgani H., 2022, Buckling analysis of three-dimensional functionally graded Euler-Bernoulli nanobeams based on the nonlocal strain gradient theory, *Journal of Applied and Computational Mechanics* **53**(1): 24-40.

[46] Li L., Hu Y., Ling L., 2015, Flexural wave propagation in small-scaled functionally graded beams via a nonlocal strain gradient theory, *Composite Structure* **133**: 1079-1092.

[47] Jalaei M.H., Civalek Ö.M.E.R., 2019, A nonlocal strain gradient refined plate theory for dynamic instability of embedded graphene sheet including thermal effects, *Composite Structure* **220**: 209-220.

[48] Ebrahimi F., Dabbagh A., 2017, On flexural wave propagation responses of smart FG magneto-electro-elastic nanoplates via nonlocal strain gradient theory, *Composite Structure* **162**: 281-293.

[49] Ma L.H., Ke L., Reddy J.N., Yang J., Kitipornchai S., Wang Y.S., 2018, Wave propagation characteristics in magneto-electro-elastic nanoshells using nonlocal strain gradient theory, *Composite Structure* **199**: 10-23.

[50] Sahmani S., Aghdam M.M., Rabczuk T., 2018, Nonlinear bending of functionally graded porous micro/nano-beams reinforced with graphene platelets based upon nonlocal strain gradient theory, *Composite Structure* **186**: 68-78.

[51] Jamali M., Shojaee T., Mohammadi B., 2020, Analytical buckling and post-buckling characteristics of Mindlin micro composite plate with central opening by use of nonlocal elasticity theory, *Journal of Applied and Computational Mechanics* **51**(1): 231-238.

[52] El Meiche N., Tounsi A., Ziane N., Mechab I., 2011, A new hyperbolic shear deformation theory for buckling and vibration of functionally graded sandwich plate, *International Journal of Mechanical Sciences* **53**(4): 237-247.

[53] Ghorbanpour Arani A., Zarei H.B.A., Haghparast E., 2018, Vibration response of viscoelastic sandwich plate with magnetorheological fluid core and functionally graded-piezoelectric nanocomposite face sheets, *Journal of Vibration and Control* **24**(21): 5169-5185.

[54] Ghorbanpour Arani A., Haghparast E., Zarei H.B.A., 2016, Nonlocal vibration of axially moving graphene sheet resting on orthotropic visco-Pasternak foundation under longitudinal magnetic field, *Physica B: Condensed Matter* **495:** 35-49.

[55] Nguyen-Xuan H., Tran L.V., Thai C.H., Kulasegaram S., Bordas S.P.A., 2014. Isogeometric anal- ysis of functionally graded plates using a refined plate theory. *Composites Part B Engineering* **64**: 222–34.

[56] Haghparast E., Ghorbanpour-Arani A., Ghorbanpour Arani A., 2020. Effect of fluid–structure interaction on vibration of moving sandwich plate with Balsa wood core and nanocomposite face sheets. *International Journal of Applied Mechanics* **12**(07): 2050078.

[57] Alipour M.M., Shariyat M., 2011, A power series solution for free vibration of variable thickness Mindlin circular plates with two-directional material heterogeneity and elastic foundations, *Journal of Solid Mechanics* **3**(2): 183-197.

[58] Najafizadeh M.M., Raki M., Yousefi P., 2018, Vibration analysis of FG nanoplate based on third-order shear deformation theory (TSDT) and nonlocal elasticity*, Journal of Solid Mechanics* **10**(3):464-475.

[59] Molla-Alipour M., Shariyat M., Shaban M., 2020, Free vibration analysis of bidirectional functionally graded conical/cylindrical shells and annular plates on nonlinear elastic foundations, based on a unified differential transform analytical formulation, *Journal of Solid Mechanics* **12**(2): 385-400.

[60] Ghorbanpour Arani A., Haghparast E., Zarei, H.B.A., 2016, Vibration of axially moving 3-phase CNTFPC plate resting on orthotropic foundation, *Structural Engineering and Mechanics* **57**(1): 105-126.

[61] Ghorbanpour-Arani A.A., Khoddami Maraghi Z., Ghorbanpour Arani A., 2023, The Frequency Response of Intelligent Composite Sandwich Plate Under Biaxial In-Plane Forces, *Journal of Solid Mechanic* **15**(1): 1-18.

[62] Mahmoudi A., Benyoucef S., Tounsi A., Benachour A., Adda Bedia E.A., Mahmoud, S.R., 2019, A refined quasi-3D shear deformation theory for thermo-mechanical behavior of functionally graded sandwich plates on elastic foundations, *Journal of Sandwich Structures and Materials* **21**(6): 1906-1929.

[63] Thai C.H., Ferreira A.J.M., Bordas S.P.A., Rabczuk T., Nguyen-Xuan H., 2014. Isogeomet- ric analysis of laminated composite and sandwich plates using a new inverse trigonometric shear deformation theory. *European Journal of Mechanics - A/Solids* **43**: 89–108.

[64] Liu Z., Wang C., Duan G., Tan J., 2019. A new refined plate theory with isogeometric approach for the static and buckling analysis of functionally graded plates. *International Journal of Mechanical Sciences* **161**: 105036.

[65] Reddy J.N., 2000. Analysis of functionally graded plates. *International Journal for Numerical Methods in Engineering* **47**(1–3): 663–84.